

# ***3D Printing of Multi-Material Hydrogels***

IIB Project Final Report by

**Lorcan Nicholls (ln356@cam.ac.uk)**

University of Cambridge, Girton College

30th May, 2024

Senior Supervisor: Prof. Yan Yan Shery Huang

Supervisor: Yaqi Sheng

---

## **Contents**

<b>① Technical Abstract .....</b>	<b>3</b>	<b>⑥ Conclusions .....</b>	<b>40</b>
<b>② Introduction .....</b>	<b>5</b>	6.1. Primary Findings .....	40
2.1. Background & Literature Review ..	5	6.2. Future Work .....	42
2.2. Project Scope .....	12	<b>⑦ References .....</b>	<b>46</b>
<b>③ Theory and Experiment Design .....</b>	<b>14</b>	<b>⑧ Appendix .....</b>	<b>48</b>
3.1. Theoretical Treatment .....	12	8.1. Appendix I: Symbols .....	48
3.2. Experimental Methodology .....	16	8.2. Appendix II: Tabular Data .....	49
<b>④ Materials and Methods .....</b>	<b>20</b>	8.3. Appendix III: Code .....	50
4.1. Apparatus .....	20	8.4. Appendix IV: Risk Assessment ....	51
4.2. Experimental Techniques .....	26		
<b>⑤ Results and Discussion .....</b>	<b>30</b>		
5.1. Analysis of Results .....	30		
5.2. Discussion .....	35		

---

**(1) Technical Abstract**

---

**3D Printing of Multi-Material Hydrogels**

**Lorcan Nicholls** (ln356@cam.ac.uk), Girton College, University of Cambridge

**Summary**

The advent of hydrogels has revolutionised biomedical science, propelling research in bioengineering and nanoscience due to their mechanically flexible, soft, and biocompatible properties. While functional materials like magnets are ubiquitous, their integration with hydrogels into composite materials remains underdeveloped despite significant potential. This project presents the synthesis, optimisation, characterisation, and applications of 3D-printable magnetic nanofiber-hydrogel composites optimised for fatigue resistance. Two applications for these composites include substrates for *in vitro* lung organoids to study mechanobiological interactions of lung epithelial cells during inspiration via programmable electromagnets, and as tissue-mimetic fillers for post-surgical cavities to prevent internal tissue adhesions. Although these applications were outside the scope of the experimentals in this project, they are a key focus of the conclusions on this project's potential applications.

**Report Structure**

The report begins with a literature review of current magnetic soft actuator technology and microfiber synthesis, followed by a theoretical analysis of the target composite system. It details the experimental procedures for modular synthesis and provides a quantitative comparison of magnetic responsiveness across various material compositions. The report concludes with a discussion on the applications, advantages, and challenges of these materials.

**Approach**

Although stimuli-responsive pure hydrogels have been known in the literature for decades, these systems rely on their intrinsic physicochemical properties, such as the effect of environmental pH, temperature and light sensitivity on the hydrogel crosslinking and ionisation. These environmental parameters must be tightly controlled in the biomedical domain to maintain cell viability both *in vitro* and *in vivo*, limiting the utilisation of this mode of actuation in soft biocompatible materials. Magnetism, as a straightforward method for applying external, no-contact forces on soft materials, with manageable cytotoxicity, was chosen as a suitable functional material to enable actuation while maintaining a homeostatic environment. This led to the development of a composite of flexible magnetic-polymer microfibers within a hydrogel matrix for soft biocompatible actuators.

A theoretical framework based on structural analysis and multiphysics simulations guided the material selection process. Experiments identified fibres with optimal magnetic responsiveness and hydrogels with suitable viscoelastic and rheological properties. Wet spinning was used to produce the fibres, and 3D bioprinting to incorporate them into the hydrogel matrix (although manual extrusion is also possible and was simpler for demonstration purposes). The fibres were encapsulated within the hydrogel in its liquid phase and solidified by cooling. The composites were tested for deflection under a switching magnetic field, evaluating sensitivity and fatigue resistance.

## **Results**

Automated wet spinning, using a robotic arm and motor-controlled spinner, produced fibres with consistent morphology. Light microscopy revealed an average fibre diameter of  $15 \pm 9$  microns, largely independent of the synthesis formula. Iron oxide ( $\text{Fe}_3\text{O}_4$ ) and polystyrene were used to create the magnetic-polymer fibres. A binary solvent of 85% *N,N*-dimethylformamide (DMF) and 15% acetone dissolved the mixture, producing fibres spun to an initial length of 28 mm. Variations in iron oxide and polystyrene concentrations (10%, 20%, 30% by weight) identified that a 40-50 wt% solid fraction yielded fully spinnable solutions, with highest magnetic responsiveness at the highest iron content. Deflection tests showed peak displacements of  $\sim 2$  mm with virtually zero time lag or hysteresis, retained with the hydrogel. The 20% polystyrene and 30% iron oxide composition was optimal for fatigue resistance and hydrogel adherence, making it the optimal choice for soft actuators in remotely stimulated applications.

## **Conclusions**

This project has demonstrated a novel synthesis of microfibre technology within soft biocompatible hydrogels with key challenges of such composites resolved, including fatigue resistance, prevention of delamination between the fibres, and prevention of cutting through the hydrogel during fibre actuation. The physical construction of the presented composite is straightforward and feasible with open-source technology, and is moreover expected to be highly biocompatible due to the separation between the inorganic magnetic fibre layer and the hydrogel in which cells may proliferate freely. This paves the way for soft actuator technology in a range of biomedical and nanoscience applications leveraging the inherent biocompatibility of the system.

---

②    **Introduction**

---

### **2.1. Background & Literature Review**

Materials designed to mimic the adaptability and flexibility of biological tissues hold immense promise for a variety of highly interdisciplinary science and engineering applications. In the recent decade, rapid progress in the fields of 3D and 4D bioprinting and responsive materials has led to the convergent development of soft functional materials which have driven research into current and emerging technologies including mechanobiology research, organoids, tissue engineering, regenerative medicine, actuators for soft robotics and smart textiles for wearable technology.

One of the key challenges relevant to many of these applications is the high standard of biocompatibility required of the constituent materials. In the realm of materials science, hydrogels occupy a distinct niche as a class of substances characterised by a cross-linked polymer network with the ability to absorb and retain substantial quantities of water, providing them with the properties of mechanical softness, flexibility, and biocompatibility [1]. While some shape-memory hydrogel formulations can be designed to exhibit an intrinsic response to stimuli such as light, temperature and pH on their own as a result of the steric and electrostatic properties arising from their physico-chemical bonding, their scope is broadened further when combined with other responsive materials, such as semiconductors [2], ferromagnets [3] [4] [5], ferroelectrics [6] and even superconductors [7]. These heterogeneous biphasic functional composites possess tunable properties by means of varying the morphology of the dispersed phase within the hydrogel into arrangements such as nanoparticles [8], nano- and microfibres, thin films and amorphous multi-material networks.

The present project undertakes an exploration into the potential of incorporating hydrogels into three-dimensionally printed magnetic composites for actuator applications. It is proposed that this synergistic combination of materials has the potential to yield actuators with enhanced performance and expanded functionality, while being manufacturable to high dimensional tolerance without the need for specialised fabrication facilities. A range of possible materials was surveyed based on both existing literature and new experimentation, and various important

properties of interest of the resulting composites are characterised and reported. The exploration of 3D printing techniques for fabricating magnetic hydrogel composites offers precise control over the material's structure, shape, and functionality, unlocking new possibilities for complex and customized actuator designs. Through this research, we aim to contribute to the advancement of soft actuator technology by developing 3D printable magnetic hydrogel composites, opening up exciting opportunities for applications in diverse fields.

In this introductory section, a summary of the main principles behind the two core components of the new composite - **magnetic fibres** and **hydrogels** - is presented, followed by a literature review of the main fabrication techniques in the laboratory and their applications across science and engineering, and finally the scope of the project throughout its development is discussed.

## Hydrogels

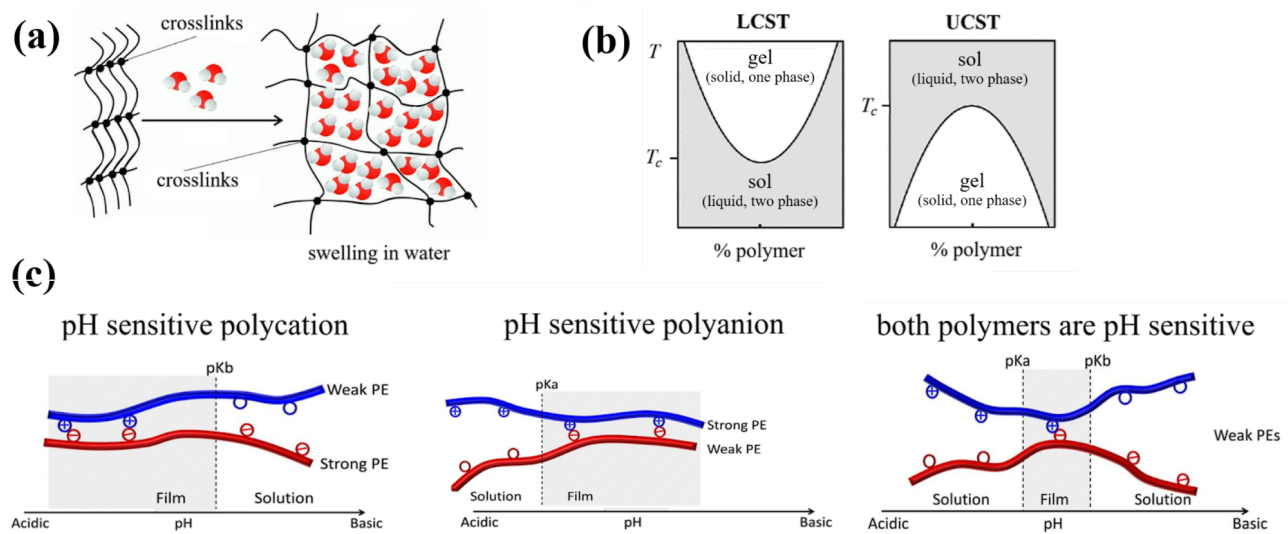


**Fig. 1.** Main principles of hydrogels. **(a)** Schematic of the swelling of crosslinked polymers due to addition of water. **(b)** The phase diagrams of LCST and UCST hydrogels, showing the sol-gel transition between the fields. **(c)** Intrinsically-responsive hydrogels showing sensitivity to pH, due to weak and/or strong ionisation of polyelectrolytes at different pH, resulting in differential swelling in solution.

Hydrogels composed of natural biopolymers are especially capable of mimicking the mechanical properties of biological tissues. These biopolymers are also polyelectrolytes, containing permanently ionised functional groups on their chains acting as hydrophilic binding sites for

solvent water molecules, ions. If the polymer contains charges of both polarities, referred to as a polyampholyte, these sites can attract each other, permitting native physical cross-linking between chains, by ionic attractions, hydrogen bonding or physical entanglement. These polymers are highly water-soluble and incorporate water molecules into their 3D structures resulting in swelling and formation of a stable solid-like polymer network. For example, in gelatin, hydrogen bonding shifts the random conformation to a structured one in which single helices associate into triple helices, bringing about the sol-gel transformation [10]. Other natural polymers with similar physical crosslinking mechanisms include agarose, alginate, chitosan, collagen, heparin, hyaluronan, fibrin and matrigel, all of which are entirely natural in origin. Synthetic hydrogels have been developed to address concerns about the durability of these materials, which use man-made polymers lacking ionisation, instead enacting their phase transition by chemical crosslinking, such as by amidation, transesterification or photocatalytic bond formation by ultraviolet radiation, as exploited by their usage as bioinks in light projection bioprinting. The most common synthetic hydrogels are based on polyethylene glycol and its diacrylate (PEGDA), modified cellulose, methacrylated gelatin (GelMA) and proprietary poloxamers such as Pluronic F-127. These are widely used when control of the rate of natural degradation is necessary, such as in tissue engineering applications, where the rate of proliferation of the host cells must closely match the rate of *in vivo* biodegradation of the matrix while retaining its mechanical stability.

Natural hydrogels can be divided into two subclasses depending on the temperature dependence of their solubility. Those in which cooling from high temperature promotes crosslinking, forming solid gels at room temperature, are classed as being ‘lower critical solution temperature’ (LCST) hydrogels, and those with the opposite behaviour have an ‘upper critical solution temperature’ (UCST), as shown in Fig. 1(b). These phase transitions occur on account of thermodynamics, due to the free energy minimisation and polymer-solvent interactions as predicted by the Flory-Huggins solution theory of polymeric colloids, where the curves shown may represent either the binodal (stable coexistence) or spinodal (metastable) phase boundaries. Whether a particular polymer forms an LCST or UCST hydrogel depends on its chemical makeup, which are tunable for synthetic hydrogels, and has great importance for their use in bioprinting, where the nozzle and stage temperatures must be set appropriately for solidification on equilibration to ambient conditions.

Natural protein-based hydrogels can also have their solubility modified by addition of simple salts to the water solution. While the precise mechanism is not fully clear, it is generally observed that ‘kosmotropic’ ions - those that promote the structuring of water through its hydrogen bonding network - result in decreased polymer solubility, such as by citrate, phosphate and tartrate salts. Conversely, the ‘chaotropic’ ions promote disorder and tend to homogenise the phases, increasing solubility, such as by potassium, ammonium and guanidinium salts. These phenomena are widely exploited in various standard molecular biology assays where they result in ‘salting out’ or ‘salting in’ of target proteins respectively. The mechanical (as well as electrical transport) properties of the resulting natural hydrogel can be tuned in this way, where addition of kosmotropic anions during gel formation results in increased hydrogel stiffness due to promoted polymer agglomeration. pH-sensitive crosslinking results in intrinsically responsive hydrogels (Fig. 1(c)), a type of functionalised hydrogel, which has inspired numerous innovative new approaches to synthesise composite materials of hydrogels to respond to other stimuli such as light, electricity and magnetism. The latter is the primary focus of this project, where the hydrogel is used as a soft substrate which is actuated by a magnetic matrix interwoven with the hydrogel.

### Magnetic Materials

Many traditional actuator applications rely on magnetism to move parts of devices, such as the simple electromagnetic relay switch, but these man-made systems are highly unsuitable for use in biocompatible applications, and indeed many of the metallic alloys used in modern industrial magnets are toxic in contact with organic tissue.

A potential point of terminology-based confusion originates from the term ‘soft’, which herein refers to the mechanically compliant nature of the hydrogel-based composites, but in the study of magnetic materials has its own meaning, namely, the class of magnetic materials that cannot sustain an internal magnetisation **M** in the absence of an external magnetic field **B**. Permanent magnetic materials are known conversely as ‘hard’ magnetic materials, develop magnetic fields as a direct result of a quantum mechanical interaction in which unpaired electron spins and electrons in orbitals with net angular momentum spontaneously align to minimise the exchange energy in microscopic regions known as magnetic domains, and are the type of ferromagnets most relevant to this project. There are only three elements on the periodic table which are hard

ferromagnets at standard conditions, namely iron, cobalt and nickel, as well as some of the rare-earth lanthanide elements often used for magnetic alloys. Unfortunately, cobalt and nickel are considerably toxic and easily oxidised, limiting their use as biocompatible magnets. Some of iron's natural mineral forms, magnetite ( $\text{Fe}_3\text{O}_4$ ) and maghaemite ( $\gamma\text{-Fe}_2\text{O}_3$ ), inherit iron's magnetism while being biocompatible, and have given rise to a 'superparamagnetic iron oxide nanoparticles' (SPIONs), in which each nanoparticle is fully magnetised to saturation in its own domain, used in medical imaging, tumour treatment and targeted drug delivery. Alterations to the surface chemistry of these particles allows further functionalisation such as in magnetic nanobiocatalysts for protein isolation in affinity chromatography. These magnetic particles retain permanent magnetisation and are a good choice for composite polymeric materials, where the iron oxide nanocrystals are present as precipitate inclusions embedded in the polymer microstructure.

### **Fibre Spinning**

For the applications relevant to this project, bulk composite materials are not the optimal choice of geometry to satisfy the delicate mechanical constraints in operation. Fibrous materials have a higher strength-to-weight ratio than for bulk materials and numerous methods have been developed to fabricate fibres of varying thickness and dimensional tolerances. Traditional methods of fibre spinning include processing the polymer from the molten state, which is useful for thermoplastics but the elevated temperatures can result in degradation in more fragile polymers, especially those relevant to functional micron-scale fibres. Instead, the polymer may be prepared in a suitable solvent, sometimes known as a 'dope', which solubilises the polymer and allows extrusion in the monophasic liquid state without the need for heating. Examples of such 'solution spinning' techniques include dry spinning, wet spinning, gel spinning and electrospinning.

Electrospinning is a useful electrohydrodynamic technique used to produce submicron diameter polymeric nanofibres within the wider range of electrospraying techniques, which has also found extensive application in nanoparticle synthesis. Under a high voltage, liquid droplets become charged and elongate through a spinneret due to electrostatic repulsion, breaking surface tension and forming a Taylor cone which permits a fine continuous flow, solidifying in flight to form

wound fibres. A modification to use two coaxial flows of liquid before emission allows synthesis of more complex compositions such as two-phase shell-and-tube structures.

A simpler method without the need for high voltage electronics is the dry spinning method, in which a background airflow is enough to evaporate the solvent bound to the polymer fibres. The dry spinning method is most suitable for high-vapour pressure polymer solutions, and is known to favour skin-core fibre morphologies as trapped solvent effuses from the interior of the fibres through micropores [11].

### **3D Printing of Soft Materials**

3D printing is a well-established, democratic (open source) and flexible additive manufacturing method for polymer-based materials, and is a popular alternative to traditional injection moulding well suited for extrusion exploiting the tunable and stimulus-triggered cross-linking of hydrogels. A more specialised extension includes so-called 4D printing, where the time-dependent response of the hydrogel to environmental stimuli can lead to pre-planned folding and migration patterns. For applications involving cell cultures, the soft material (a ‘bioink’) may contain live cells in a hydrogel-biomolecule formulation, either as the fully-formed scaffold, or its precursors (controlled induced cross-linking). One of the principal applications utilising these technologies that is most relevant to the potential extensions of this project is regenerative medicine, an emerging field in biomedical science that widely incorporates 3D printing of soft materials, involving the *in vivo* formation of personalised tissues such as skin, bone and organ tissue. To match physiological environmental conditions the hydrogel may be prepared with phosphate-buffered saline (PBS) instead of deionised (DI) water as the swelling medium. In order to successfully integrate with the host tissue, implanted tissues must contain a matrix (a 3D polymeric scaffold structure mimicking the natural extracellular matrix), signalling molecules (biomolecules such as growth factors and Yamanaka factors to signal stem cell reversion to the pluripotent state) and live cells, depending on the type of tissue to be regenerated. An alternative cell-free approach to tissue engineering involves removing cells from the formulation, and instead using ‘homing’ of host cells into the new scaffold, promoted by the biomolecules. 3D printing of such materials requires a robust deposition method to handle the highly complex formulation properties, with dedicated bioprinters being developed to address

these demands. Bioprinting can be done by various methods, adapted from and inspired by the approaches in conventional 3D printing:

- Extrusion: continuous deposition of a viscous bioink stream from a syringe.
- Inkjet: directed emission of bioink droplets from a piezoelectric nozzle.
- Projection: UV-radiation-initiated cross-linking of photosensitive hydrogels

The rheological properties of the bioink (gelation kinetics, surface tension, viscoelasticity, shear-dependent and time-dependent viscosity) are important design parameters, depending on the printing method. The addition of cross-linkers into the bioink allows the solidification of the hydrogel in the scaffold once deposited. Depending on whether the hydrogel is UCST or LCST, either the syringe or stage must be heated to form the gel before deposition. The cells can be supported on microcarriers suspended in the bioink, which are made of either natural (cellulose, gelatin, collagen) or synthetic (e.g. dextran, plastic, glass) hard materials. This arrangement permits high cell counts to be used without compromising viability, as well as improved nutrient exchange. Some types of cell e.g. chondrocytes can help to replace the scaffold with new ECM tissue if rigidity is desired. Functional materials (e.g. graphene, magnetic fibres, metal nanoparticles) can also be supplied in the bioink with careful control of suspension rheology, orientation and biocompatibility.

The composite systems developed in this project were informed by successful multi-material systems found in the literature as well as those known to be compatible with the equipment available in the Nanoscience Centre at University of Cambridge.

### **Magnetic Fibres**

It is only in the past few years that soft multi-material composites of magnetic materials have been conceptualised and appreciated for their scope of applications. A comprehensive 2020 review [14] describes the wide range of materials compatible with magnetic fibres, outlines a mathematical theory of their material properties and discusses the combination with hydrogels and use with live cells as a highly relevant application.

In [13], highly flexible 300 µm diameter

In [12], 500 µm diameter SmCo<sub>5</sub> fibres were produced by mixing with polystyrene in toluene, showing a peak tensile strength of 450 MPa. The use of lanthanide alloys likely makes this composition too expensive for widespread use in smart textiles, but illustrates the feasibility of wet-spinning magnetic materials into flexible fibres through the use of a polymeric filling.

## **Printable Hydrogels**

### **Comparison of Fibre Spinning Techniques**

### **Applications of Magnetic Hydrogel Composites**

### **2.3. Project Scope**

#### **Initial Goals and Context**

#### **Revised Project Goals**

### ③ Theory and Experimental Design

#### 3.1. Theoretical Treatment

In this project, the magnetic fibres are modelled as elastic beams constrained at their ends to represent the overhanging and underhanging sections spun around the frame. The fibres are subject to their own self-weight and a magnetic force in the transverse direction hanging in a compliant hydrogel medium.

#### Structural Mechanics

A simplistic analysis of the setup used to test the fibre composites is initially performed using static Euler-Bernoulli beam theory. In this model, the stiffness of the hydrogel is presumed to be sufficiently low to not resist the deflections of the fibre, and the resultant deflection of the hydrogel is decoupled from the fibre. Due to adhesion of the fibre to the surface of the horizontally-oriented frame at each end, the fibres are effectively clamped at each end, as depicted in Figure 2. This system is now a linear superposition of a statically indeterminate beam and a uniformly distributed load (UDL) which can be solved for the shear forces  $S(x)$ , bending moments  $M(x)$  and transverse displacements  $y(x)$  by equilibrium with the load per unit length  $w(x)$  and compatibility  $dy/dx = 0$  at  $x = -l/2$  and  $x = l/2$ .

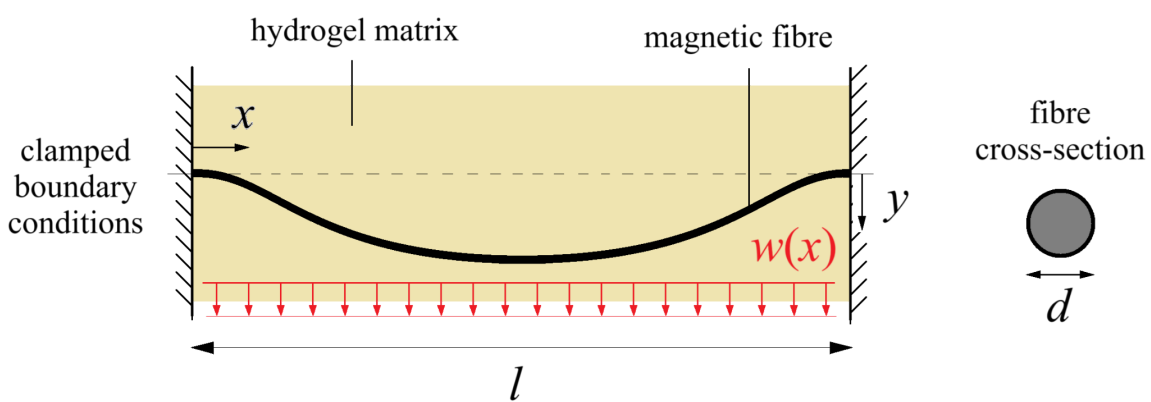


**Fig. 2.** Diagram of the magnetic fibre modelled as a structurally elastic element clamped between two supports separated by a distance  $l$ . The shape of the displaced fibre  $y(x)$  is illustrated. A simple solid circular cross-section of a fibre is shown with diameter  $d$ .

For fibres spun to a length  $l$  between supports, with no contraction, with Young's modulus  $E$ , second moment of area  $I$  (flexural rigidity  $EI$ ), the clamping moments at the ends of the fibre are

$$M(-l/2) = M(l/2) = \frac{wl^4}{12} \quad (\text{Equation 1})$$

To determine expressions for  $S(x)$ ,  $M(x)$  and  $y(x)$ , we consider a linear superposition starting with a statically determinate simply-supported beam under a UDL  $w(x)$ , apply the necessary moment to enforce compatibility with zero angle at the ends and solve the equilibrium equation. The resulting expressions of this analysis are:

$$S(x) = \frac{dM}{dx} = wx \quad (\text{Equation 2.1})$$

$$M(x) = -EI \frac{d^2y}{dx^2} = \frac{w}{2} \left( x^2 - \frac{L^2}{12} \right) \quad (\text{Equation 2.2})$$

$$y(x) = \frac{w}{384EI} (8L^2x^2 - 16x^4 - L^4) \quad (\text{Equation 2.3})$$

From this, it is observed that the bending moment in the fibre does not exceed the clamping moments, and the maximum displacement can be found:

$$M_{max} = \frac{wl^4}{12} \text{ at } x = \pm \frac{l}{2} \quad \text{and} \quad y_{max} = \frac{wl^4}{384EI} \text{ at } x = 0 \quad (\text{Equation 3})$$

The intended applications of these magnetic fibres will be expected to involve cyclic loading of the magnetic field, hence making fast fracture due to fatigue a critical failure mode of the fibres, occurring at lower stresses than at plastic yield. It is commonly accepted that the maximum high-cycle fatigue design stress, for infinite cycles to failure, for many materials is approximately half of the yield strength  $\sigma_y$ , which places an upper bound on the maximum load  $w$  from Equation 3. If the second moment of area for the circular cross-section is  $I = \pi d^4/64$ , the maximum allowable stress  $\sigma_y/2$  then applying  $\sigma = My/I$  gives an upper bound on the allowable magnetic force per unit length to prevent fatigue-induced failure:

$$\frac{16wl^2}{3\pi d^3} \leq \sigma_y \quad \Rightarrow \quad w \leq \frac{3\pi}{16} \frac{d^3 \sigma_y}{l^2}. \quad (\text{Equation 4})$$

## Hydrogel Deformation

With an estimate of the fibre deflection  $y(x)$  in Equation 2.3, the effects of the hydrogel can now be investigated. While a rigorous analysis might involve modelling the hydrogel as a continuum subject to a line of prescribed deformations due to the fibre, a simpler method is to modify the plane strain elastic beam model by incorporating a continuous distributed viscoelastic reaction force across the fibre representing the contact with the hydrogel, based on a Kelvin-Voigt linear viscoelasticity model. At steady state, the viscosity of the hydrogel does not contribute a force, and the equilibrium condition simplifies to the Winkler support model [17], given by:

$$EI \frac{\partial^4 y}{\partial x^4} + \eta \frac{\partial y}{\partial t} + ky(x, t) = w(x, t) \xrightarrow[\dot{y} = 0]{\text{steady-state}} EI \frac{\partial^4 y}{\partial x^4} + ky = w \quad (\text{Equation 5})$$

where  $k$  is the stiffness of the hydrogel per unit length. Equation 5 was solved using Python's `scipy.integrate.solve_bvp` function in terms of the characteristic reciprocal length

$\lambda_w = \sqrt{\frac{k}{4EI}}$ , so that  $\frac{d^4 y}{dx^4} + 4\lambda_w^4 y = \frac{w}{EI}$  with boundary conditions  $y(\pm\frac{l}{2}) = 0$  and  $\frac{dy}{dx}(\pm\frac{l}{2}) = 0$ .

This allows us to examine the effect of the stiffness-to-rigidity ratio  $k / EI$  on the maximum displacement, where the model reduces to Equation 2.3 in the case of  $k = 0$  (no hydrogel).

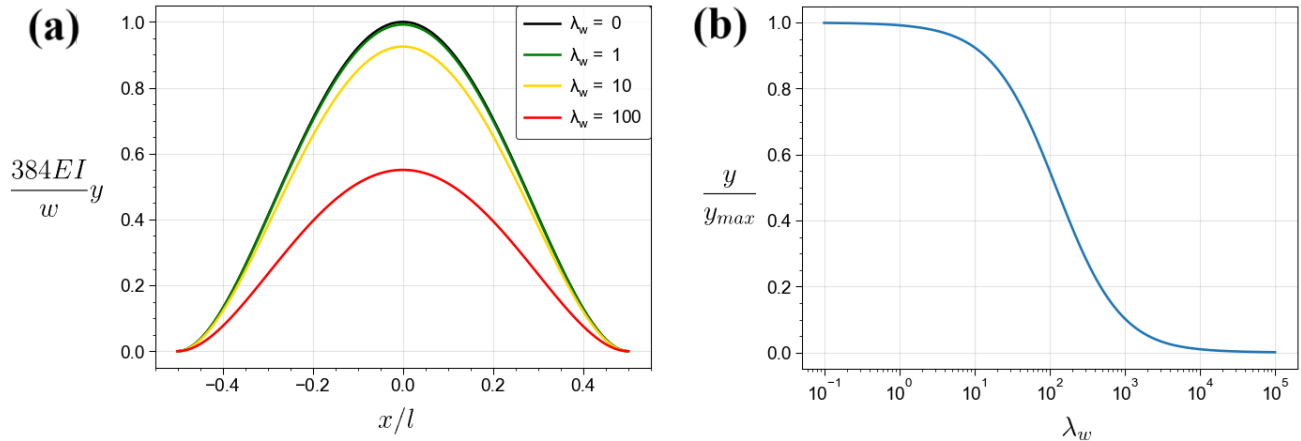


**Fig. 3. (a)** Displacement  $y(x)$  of a magnetic fibre based on Equation 5 for a variety of hydrogel-to-fibre stiffness ratios (dimensions of  $\lambda_w$ :  $\text{L}^{-1}$ ) illustrated with  $w = 1$ ,  $EI = 1$  and  $l = 1$ . The ‘no hydrogel’ case is marked in black. **(b)** Knockdown factor in peak displacement at  $x = 0$  for a wide range of  $\lambda_w$ , showing little impact for  $\lambda_w < 10$ , and immobilising the fibre for  $\lambda_w > 1000$ .

## Magnetic Force

We now need to estimate the magnetic force loading. A finite element of a hard ferromagnetic material possessing internal magnetisation  $\mathbf{M}$ , exposed to an external magnetic field of flux density  $\mathbf{B}$ , experiences a resultant force  $\mathbf{F}$  and torque  $\boldsymbol{\tau}$  per unit volume of material:

$$\mathbf{F} = \nabla(\mathbf{M} \cdot \mathbf{B}) \quad (\text{Equation 6.1})$$

$$\boldsymbol{\tau} = \mathbf{B} \times \mathbf{M}. \quad (\text{Equation 6.2})$$

If the field  $\mathbf{B}$  is approximately unidirectional and parallel to  $\mathbf{M}$ , and oriented with the North-South axis perpendicular to the fibre (in the  $z$ -axis direction), then Equation 6.1 simplifies:

$$\mathbf{F}_{mag} = M_0 \frac{dB_z}{dz} \hat{\mathbf{k}} \quad (\text{Equation 7})$$

where  $\mathbf{M} = M_0 \mathbf{k}$  is the magnetisation aligned in the  $\mathbf{k}$ -direction ( $z$ -axis), and the torque  $\boldsymbol{\tau} = \mathbf{0}$  as expected from a soft magnetic material (or a hard magnetic material at equilibrium).

The magnetic field surrounding a solenoid electromagnet can be represented as that surrounding a cylindrical ferromagnet with current-dependent magnetisation  $M_z$ . For a solenoid of radius  $R$ , height  $L$ , and magnetomotive force (ampere-turns)  $NI$ , this is given by the total magnetic moment per unit volume,  $M_z = \pi N I R^2$ . By solving the relevant Poisson's equation with a suitable magnetostatic potential, the external  $\mathbf{B}$ -field on the magnetisation axis can be found [15]:

$$B_z(z) = \frac{1}{2} M_z \mu_0 \left( \frac{\frac{L}{2} - z}{\sqrt{(\frac{L}{2} - z)^2 + R^2}} + \frac{\frac{L}{2} + z}{\sqrt{(\frac{L}{2} + z)^2 + R^2}} \right) \quad (\text{Equation 8})$$

Differentiating Equation 8 with respect to  $z$  and substituting into Equation 7 gives an expression for the magnetic force:

$$F_{mag} = 4\pi NI \mu_0 M_0 R^4 \left( ((L + 2z)^2 + 4R^2)^{-3/2} - ((L - 2z)^2 + 4R^2)^{-3/2} \right) \quad (\text{Equation 9})$$

The force is dependent on the displacement  $z$  of the fibre, leading to a complex coupling with no analytical solution. However, if it is presumed that  $\Delta y = \Delta z \ll L$ , then these second-order effects

can be neglected and an approximate solution can be obtained. The graph of the semi-normalised force  $\frac{-F_{mag}}{NI\mu_0 M_0}$  (dimensions: L) against  $\frac{z}{L}$  for different aspect ratios  $\frac{R}{L}$  with a basis of  $L = 1$  is shown in Figure 4, where it is observed that there is generally a peak in  $F_{mag}$  at some distance  $z > \frac{L}{2}$  from the centre of the magnet, representing a small distance away from the electromagnet surface. A magnetic fibre placed here would, assuming constant  $M_0$ , experience the maximum possible force. It is also found that short and stubby electromagnets (larger  $\frac{R}{L}$ ) produce higher maximum forces at this optimal distance.

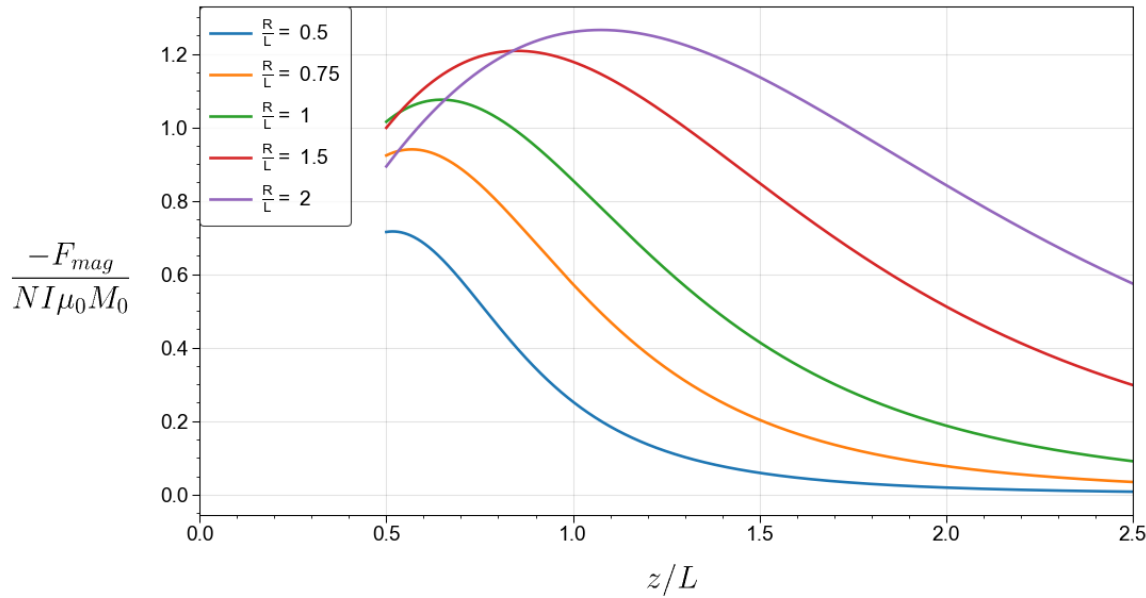


**Fig. 4.** Plot of force on a magnetic fibre at distance  $z$  from the centre of an electromagnet with radius  $R$  and length  $L$ , using Equation 9, for different ratios  $R/L$  with  $L = 1$ .

The position  $z/L = 0.5$  represents the end surface of the electromagnet.

To obtain an estimate of  $M_0$ , we require the magnetic properties of the fibres. Referring to the *B-H* characteristic curve for  $\text{Fe}_3\text{O}_4$  nanoparticles in poly(styrene-divinylbenzene) matrix obtained in [16], a saturation magnetisation of approximately  $80 \text{ A m}^2 \text{ kg}^{-1}$  (per kilogram of  $\text{Fe}_3\text{O}_4$ ) is easily attained in the fibre for applied fields above  $H > 500 \text{ A/m}$  (corresponding to  $B > 670 \mu\text{T}$ ). Lower bound estimates based on Equation 8 produce fields within the range necessary to achieve saturation for all feasible distances ( $\frac{1}{2} < \frac{z}{L} < 1$ ), so the assumption of constant  $M_0$  (per unit concentration of iron) is deemed appropriate.

## Composite Properties

Based on a simple rule of mixtures, lower and upper bounds can be established for the modulus and yield stress of an anisotropic composite, corresponding to the extreme cases of parallel and perpendicular fibres. This technique can be applied both to the hydrogel-fibre composite as well as the fibre itself. The moduli  $E$  and yield strength  $\sigma_y$  of the matrix (subscript  $m$ ) and fibres (subscript  $f$ , fracture strength  $\sigma_y^{(f)}$ ) in terms of the volume fraction of fibres  $V_f$  by

$$\underbrace{\left( \frac{V_f}{E_f} + \frac{1 - V_f}{E_m} \right)^{-1}}_{\text{modulus transverse to fibres}} \leq E \leq \underbrace{V_f E_f + (1 - V_f) E_m}_{\substack{\text{modulus parallel} \\ \text{to fibres}}} \quad (\text{Equation 10.1})$$

$$\sigma_{ts} = V_f \sigma_y^{(f)} + (1 - V_f) \sigma_y^{(m)} \quad (\text{Equation 10.2})$$

Since the hydrogel-fibre composite is to be actuated transverse to the fibres, it is appropriate to take the lower bound of Equation 10.1 for its effective modulus. Since this expression is a harmonic mean of the component moduli weighted by volume fractions, the most compliant component dominates, and so the composite modulus can be considered equal to that of the hydrogel ( $E \ll 1$  MPa). A naive estimate for the fibre modulus could use the upper bound, expressing in terms of mass fractions  $m_f$  and densities (Equation 11.1), but in reality the complex amorphous fibre requires experimental testing, which was not performed in this project. In the literature [20], up to a 300% increase in Young's modulus and 60% increase in tensile strength is known in polypropylene fibres when combined with 20 wt% iron oxide microparticles of diameter less than 33  $\mu\text{m}$ , highlighting the high sensitivity to the presence of these magnetic materials.

$$E_{\text{composite}}^{(\perp)} = \left( \frac{V_f}{\frac{m_p}{\rho_p} E_p + \left(1 - \frac{m_p}{\rho_p}\right) E_m} + \frac{1 - V_f}{E_{\text{hydrogel}}} \right)^{-1} \quad (\text{Equation 11.1})$$

$$\sigma_{ts,\text{composite}}^{(\perp)} = V_f (V_p \sigma_y^{(p)} + (1 - V_p) \sigma_y^{(m)}) + (1 - V_f) \sigma_y^{(\text{hydrogel})} \quad (\text{Equation 11.2})$$

Since  $E_{\text{hydrogel}} \ll E_m, E_p$ , then  $E_{\text{composite}}^{(\perp)} \approx E_{\text{hydrogel}}$ , and the composite strength is a sum of weighted contributions from the polymer ( $p$ ), magnetic material ( $m$ ) and hydrogel.

## Material Selection

Based on the literature review and advice from my supervisor, a shortlist of candidate materials serving the purpose of fibre spinning solvent, fibre filler polymer, fibre magnetic material and hydrogel matrix was prepared:

	Fibres		Hydrogels
Spinning solvents	Filling polymers	Magnetic materials	
<i>N,N</i> -dimethylformamide (DMF)	poly(ethylene oxide) (PEO)	iron(II, III) oxide ( $\text{Fe}_3\text{O}_4$ )	gelatin
acetone	polystyrene (PS)	neodymium alloy ( $\text{Nd}_2\text{Fe}_{14}\text{B}$ )	sodium alginate
	polyurethane (PU)	samarium-cobalt alloy ( $\text{SmCo}_5$ )	

**Table 1.** Materials considered for the synthesis of the magnetic fibre composite.

Considering that the purpose of the fibre composite is to attain deflections with high sensitivity to the magnetic field without yielding, this can be stated as a stiffness-limited design problem with an additional component accounting for magnetisation. In terms of the purely mechanical properties, we aim to maximise the performance index  $\sigma_y^2 / E$  ( $\sigma_y$ : yield stress,  $E$ : Young's modulus). A preliminary inspection of the CUED Materials Databook showed that polymers and materials based on natural materials are optimal for this design criterion. Ansys Granta EduPack (ver. 2022 R2) was then used to conduct a wider search across the Level 3 Database of materials, summarised in the materials property chart in Figure 5, allowing a closer inspection of the feasible materials used to construct the fibres. The green dashed line has gradient 2 on the log-log axes, representing the contours of the performance index function, maximised below the line. The magnetic materials are typically non-technical ceramics (e.g. iron oxide) or metals (e.g.  $\text{SmCo}_5$ ). The bubbles for 'elastomers' (light blue), 'natural fibres' (light brown) and 'fibres and particulates' (grey/black) contain the maximum values of this performance index, indicating their optimality in this material selection task.

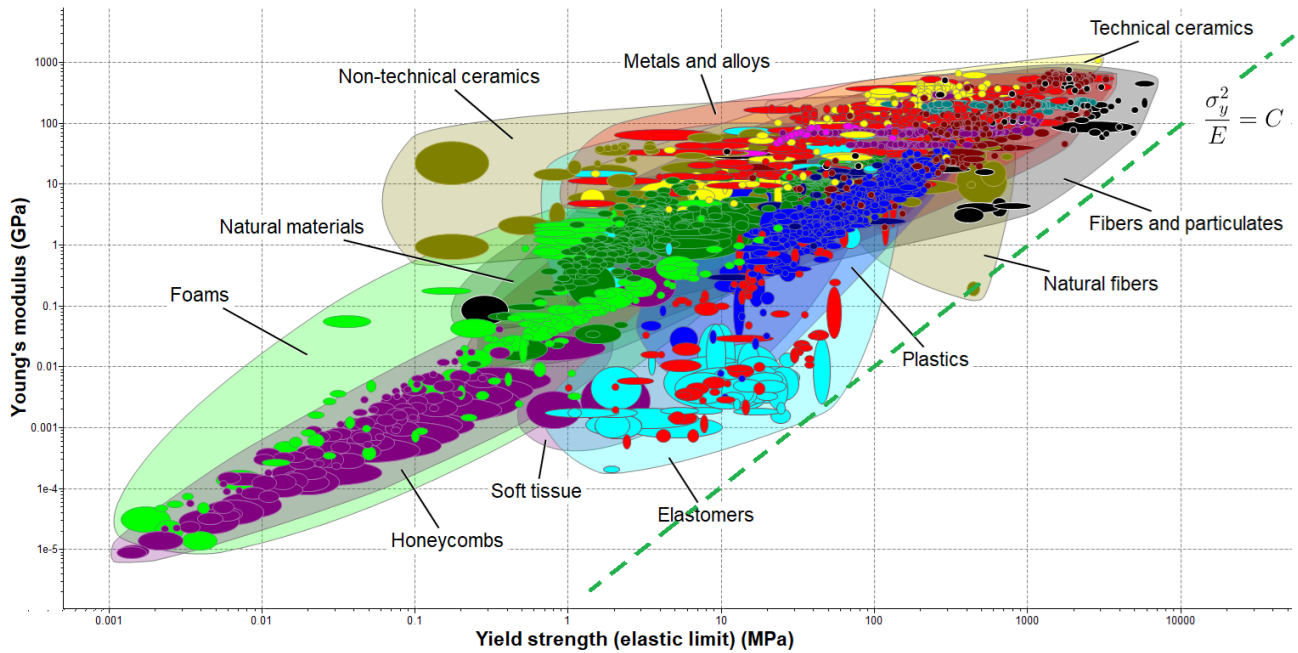


**Fig. 5.** Material property chart of yield strength  $\sigma_y$  [MPa] against Young's modulus  $E$  [GPa] for a wide range of materials, obtained from the Level 3 Database in Ansys Granta EduPack.

### Computational Modelling (Finite Element Analysis)

The theory discussed thus far is only intended as a rough approximation, and the inherently large fabrication variability of the constituent materials limits precise predictions of experimental observations, and are instead intended as tests for feasibility of such a magnetic hydrogel composite construction. A more robust (but still imperfect) method is the use of computational modelling. In this project, the CAD software SOLIDWORKS (ver. 2022) was applied extensively to prepare models of the hardware used in the experiments, and also as structural mechanics solver using the ‘Static Study’ tool under the ‘Simulation’ tab in SOLIDWORKS. Using a representative fibre diameter of  $d = 15 \mu\text{m}$ , with each fibre as a single closed loop around the frame for modelling simplicity, the schematic in Figure 6 was created. Due to the unnecessary computational complexity of modelling all fibres, this model is only presented for graphical illustration and a reduced model is used to carry out simulation studies. Detailed dimensioning information for the frame can be found in Section 4.1, and the object under study is shown in Figure 7. The assembly shown in Figure 7 is comprised of three parts (supports, fibre, hydrogel) with suitable contact and parallel separation mates applied.

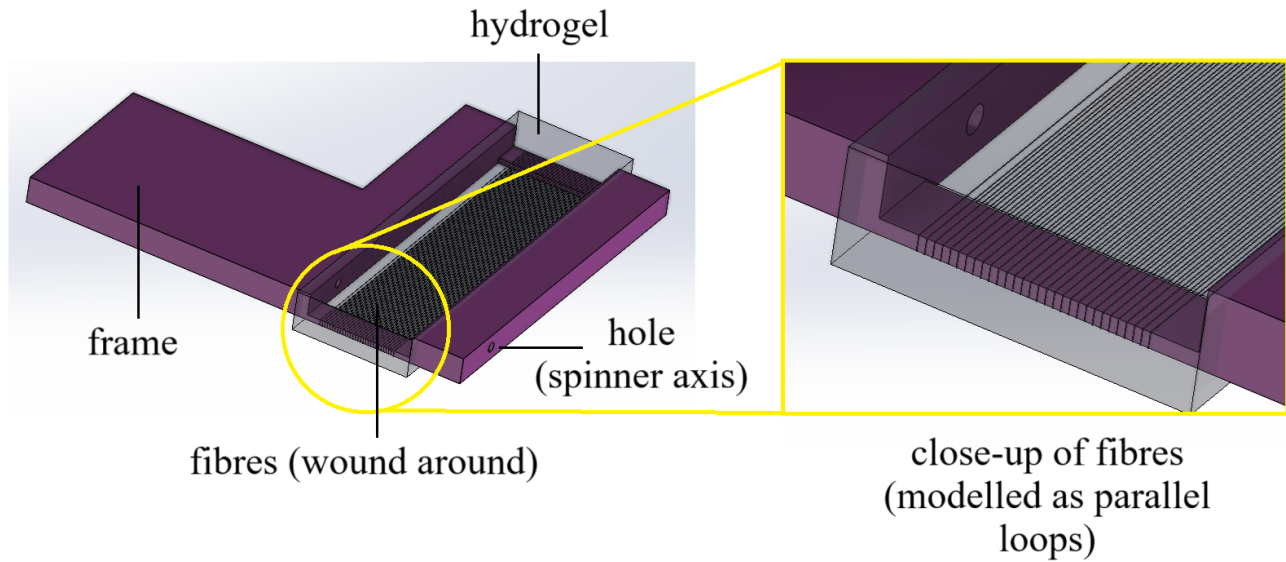


**Fig. 6.** SOLIDWORKS model of the fibres on the frame. Using a linear pattern, 30 parallel loops representing fibres (black) were placed on the frame (purple), each of diameter  $\varnothing 15 \mu\text{m}$ , covering a distance along the frame of 6 mm (separation 0.2 mm). The end-to-end length of each fibre section is 28 mm. The hydrogel (clear, grey) is represented as a cuboid covering the fibres and frame completely and extending above and below by an additional 0.5 mm.

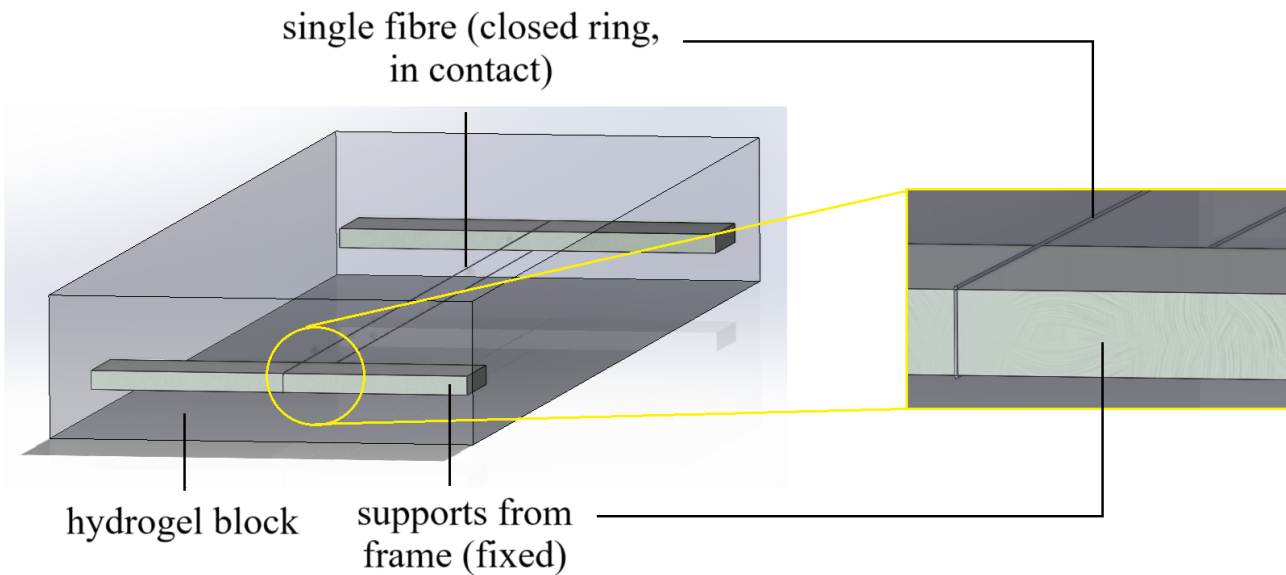


**Fig. 7.** SOLIDWORKS model of a single closed loop representing a fibre (diameter  $\varnothing 15 \mu\text{m}$ ), a horizontal distance of 28 mm across. The support cross-section is  $0.4 \text{ mm} \times 2.0 \text{ mm}$ .

In the SOLIDWORKS static study, material properties were assigned to each part. The hydrogel provides the largest source of uncertainty since its properties are highly variable, and information in the literature is generally scarce for any particular composition of hydrogel, so the Young's modulus  $E$  was deduced using nonlinear least-squares from Table 1 in [18] to estimate a 6% gelatin, 1% alginate hydrogel as used in practice for one of the experiments, finding  $E = 570$  kPa as a reasonable value. The model estimation is described in Appendix II. The Poisson's ratio was assumed to be 0.49 (almost fully incompressible, typical for rubbery substances) and the shear modulus was computed using  $G = E / (2(1 + \nu))$ . The tensile strength was estimated from a 4% gelatin hydrogel in 10 mM NaCl in [19], likely with large variation. Two UDLs of 1 mN total force were applied vertically to each lengthwise fibre section, and a custom high-quality mesh with minimum element size 0.009 mm was generated to properly capture the morphology of the micron-scale fibres. The simulation was run with the 'large displacements' flag, taking 15 minutes to solve completely consuming a peak of 4 GB of RAM. The resulting deformed structure is shown in Figure 8, with a maximum displacement of 0.688 mm.

Part	Material	Mechanical properties				
		$\rho$ [kg m <sup>-3</sup> ]	$E$ [Pa]	$G$ [Pa]	$\nu$ [-]	$\sigma_y$ [Pa]
supports	Alloy Steel	7700	$2.1 \times 10^{11}$	$7.9 \times 10^{10}$	0.28	$6.204 \times 10^8$
fibre	PS Medium/High Flow	1040	$2.28 \times 10^9$	$8.173 \times 10^8$	0.387	$3.59 \times 10^7$
hydrogel	[custom material]	1000	$5.7 \times 10^5$	$1.9 \times 10^5$	0.49	4290

**Table 2.** Material properties assigned to each part in SOLIDWORKS.

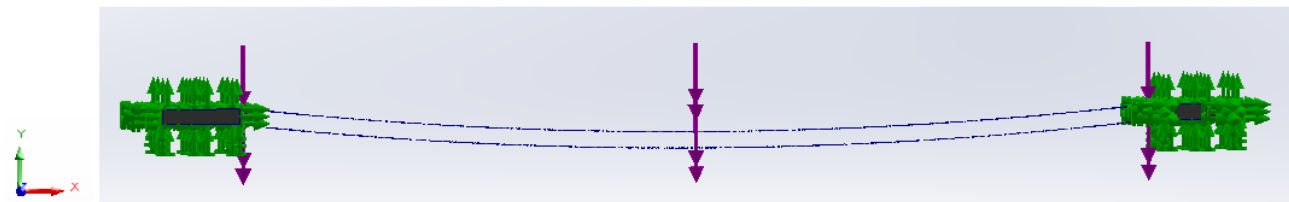
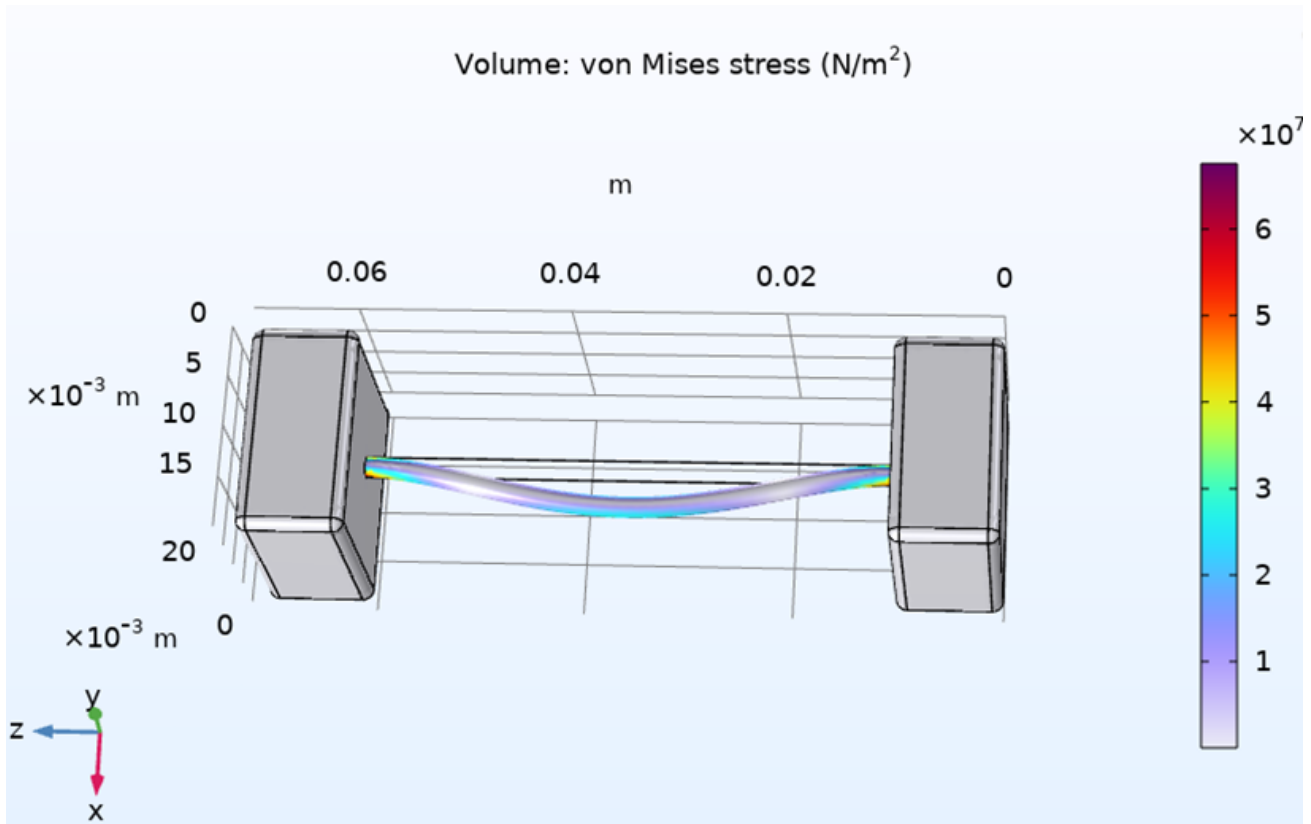


**Fig. 8.** Displaced structure under a 1 mN load. The hydrogel is hidden from view since its displacement was negligible. A central displacement of 0.7 mm is found.

Although the SOLIDWORKS study seemed reasonable based on experimental experience, a theoretical estimate based on Equation 3 yielded unrealistically large displacements, suggesting that the applied force perhaps does not reflect the true magnetic forces experienced in practice.

Next, to study the actual magnetomechanical interactions of the model, COMSOL Multiphysics (ver. 6.2) was employed to check for consistency and reliability of modelling. The SOLIDWORKS models of each part were imported into COMSOL, and a study including the Solid Mechanics (solid interface) and AC/DC (magnetic fields, no currents, boundary elements interface) physics modules with 3D geometry was prepared.



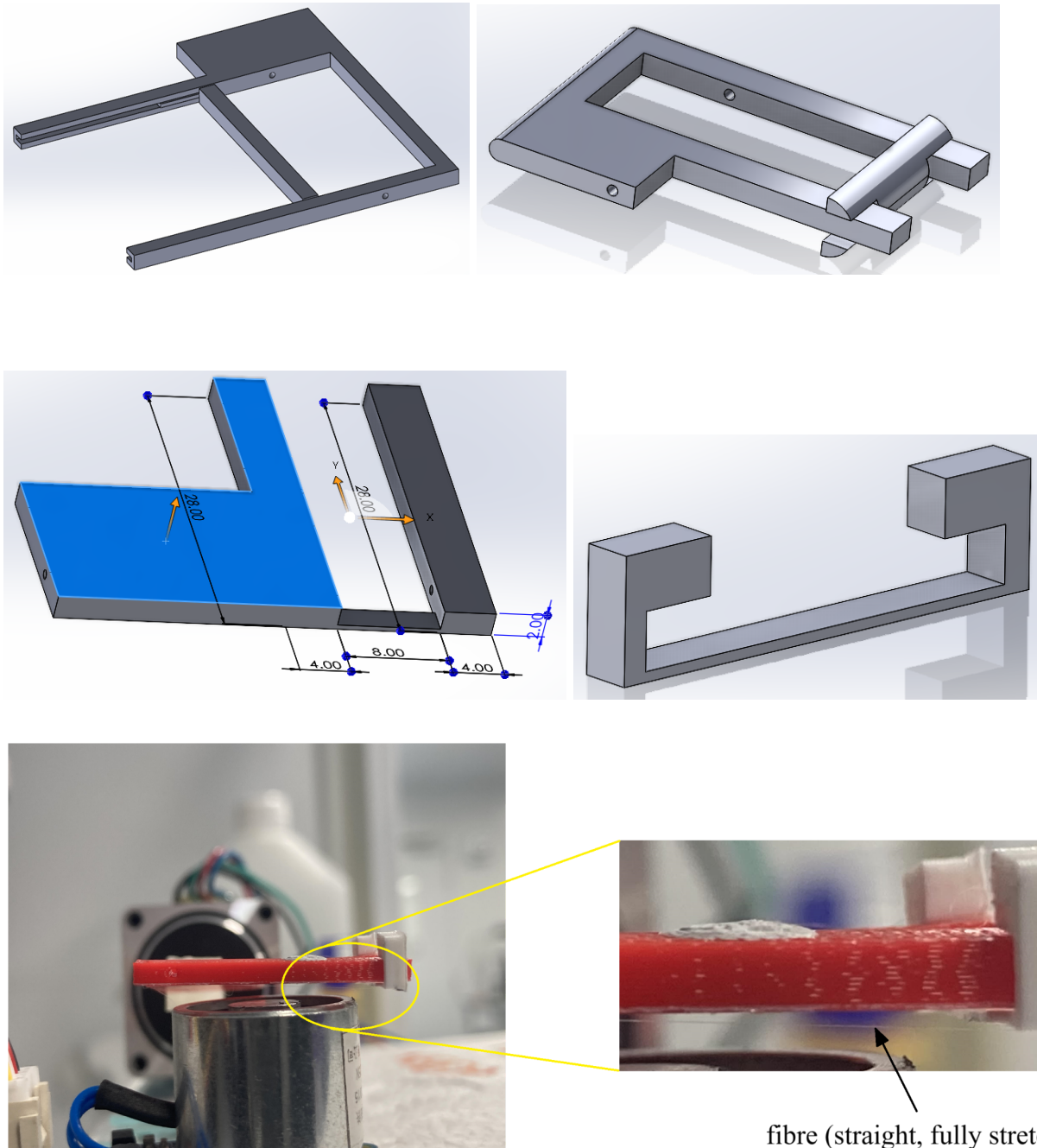
### **3.2. Experimental Methodology**

---

## ④ Materials and Methods

---

### 4.1. Apparatus



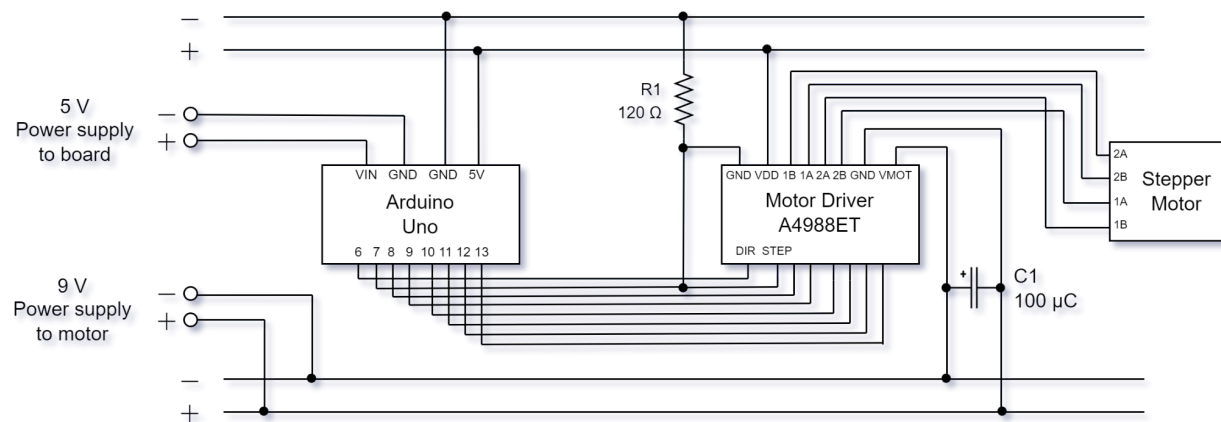
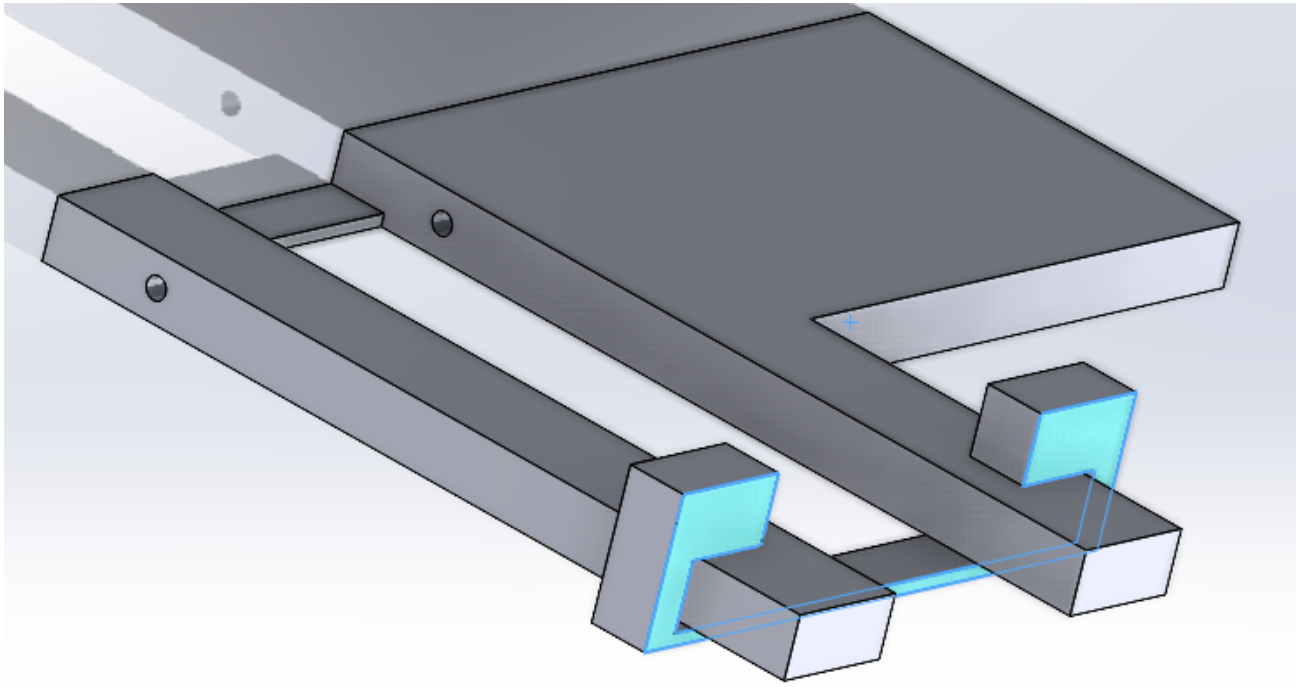


**Fig. 1.** Circuit schematic for the spinner, using an Arduino-controlled stepper motor.

## 4.2. Experimental Techniques

### Preparing Spinning Solutions

The following procedure was used to prepare each fibre solution:

1. Place a clean, dry, small capped glass vial on a balance to measure its dry mass.
2. Working inside a microbiological safety cabinet (MBSC) with a HEPA filter, place down the uncapped glass vial and the solvent containers of DMF and acetone.
3. To the glass vial, add 850  $\mu\text{L}$  of DMF using a precision micropipette; dispose of the tip.
4. To the glass vial, add 150  $\mu\text{L}$  of acetone using the micropipette; cap the vial.
5. Weigh the filled glass vial on the balance and record the mass; calculate the mass of the 1000  $\mu\text{L}$  solvent by difference; place the vial back in the MBSC. Record this as  $m_0$ .
6. Calculate the appropriate masses of polymer and iron oxide necessary to achieve a final composition of 100x wt% polymer and 100y wt% iron oxide using Equation 12:

$$\text{mass of polymer} = \frac{xm_0}{1 - (x + y)}; \quad \text{mass of iron oxide} = \frac{ym_0}{1 - (x + y)} \quad (\text{Equation 12})$$

7. Place a clean plastic weighing boat on the balance; tare (zero) the balance.
8. Using tweezers, pick and place the appropriate mass of polymer beads into the weighing boat, aiming to get as close as possible to the target mass.
9. Using a spatula, carefully weigh out the appropriate mass of iron oxide powder into the weighing boat.
10. In the MSBC, funnel the polymer beads and iron oxide powder into the solvent vial.
11. Drop in a small magnetic stir bar; cap the vial; seal the cap with Parafilm; label the vial with the composition of the solution.
12. Place a blob of Blu-tack on the bottom of the vial and stick the vial to the centre of a hot plate, heating at 50 °C and using the magnetic stirrer at a low power for approximately 2 hours to produce a viscous homogeneous black solution. The solution can be used to spin fibres straight from the heated state, or from cooling (though ideally with a little reheating to ensure full solubility).

Nine different compositions of fibre solutions were prepared, as shown in Table 3.

Identifier	Polystyrene, wt%	Iron oxide, wt%	Solvent
(1)	10	10	
(2)	20	10	
(3)	30	10	
(4)	10	20	
(5)	20	20	85 v% DMF + 15 v% acetone
(6)	30	20	
(7)	10	30	
(8)	20	30	
(9)	30	30	

**Table 3.** Compositions of the nine fibre solutions prepared and studied.

### Automatic Wet Spinning of Fibres

Once a fibre solution had been prepared, the following procedure was used to prepare a frame holding fibres across its length:

1. Working inside an MSBC, get a frame and slider, produced from the 3D printer; attach the slider on the ends of the ‘fork arms’ of the frame (at full length).
2. Set up the laptop running the uArm spinner Python program (Appendix III) and connect to the uArm robot arm. Turn on the power source for the Arduino-powered spinner. Push the pole of the spinner through the holes in the frame to make it spin on its axis. Using the command line inputs, position the robot arm approximately 5 cm directly above the spinning frame, aligned with the right-hand edge of the frame as accurately as possible.
3. Unseal and uncap the desired fibre solution glass vial, and carefully draw up approximately 1 ml of the solution into an uncapped syringe, and then quickly cap the syringe with a 25-gauge needle; re-cap and seal the glass vial. Place the syringe vertically into the hole in the robot arm end effector tool, resting in place ready for extrusion.
4. Start the Python program, which begins slowly moving the robot arm from side to side across the range of the frame interior (the range over which fibres will be spun).
5. Gently press the syringe plunger to extrude a tiny piece of the solution from the syringe tip. Using either sharp tweezers or the experimenter’s own gloves, touch the extruded

piece, allowing it to adhere and pull the piece out of the syringe. The piece will bring out a continuous fibre which can be moved onto the spinning frame below. If a good composition is chosen, the fibre will now extrude automatically from the syringe, forming fibres on the frame. Once a suitable density of fibres is attained on the frame, remove the spinner carefully and stop the robot arm program. Place the frame into a clean dry petri dish, leaving it open in the MSBC to allow any adsorbed solvent to evaporate.

6. Place the petri dish under a light microscope for characterisation of fibre quality.

The spinning technique took some trial and error, and was a significant source of ‘lost time’ during the course of the project, with many early attempts failing to produce any fibres at all, but was eventually mastered for consistently spinnable solutions. Some compositions were always challenging to spin, breaking off quickly and not spinning for more than a few seconds, making their fibres low quality.

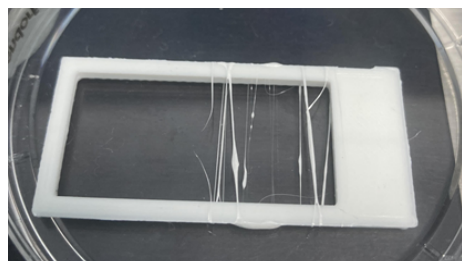


**Fig. 11.** An early attempt at spinning fibres onto a simple rectangular fixed frame, using a 30 wt% polystyrene spinning solution (no magnetic particles). The fibres were spun by hand, without the aid of a spinner or robot arm. The fibres are blobby, highly variable in thickness and some have split due to the low quality technique.

### Calculating Fibre Width

Each frame was imaged under light microscopy at 20 $\times$  magnification and saved as a digital image of dimensions 3226  $\times$  3024 pixels. A reference scale bar of size 180  $\mu\text{m}$  was displayed in all images, rendered at a constant width of 711 pixels in the digital image, enabling accurate determination of the widths of the fibres. Each frame was manually moved to a number (between 2 and 6, depending on how many fibres are present) of different locations under the imaging lens to capture a representative range of the fibres within a frame. The images were then randomly sampled to produce 10 measurements along the fibres to produce an estimate of the mean and standard deviation in the fibre width. This simple data analysis was performed in Python, reading from Excel data via the `pandas` library.

## Testing Magnetic Responsiveness

An electromagnet was added to the Arduino circuit board, programmed to turn the electromagnet on and off forever, at 9 V DC and limiting current draw, at 1 second intervals (50% duty cycle). A phone holder designed to fit into the robot tool holder was 3D printed. My iPhone was used for photo and video recording, using the robot arm to hold a position parallel to the frame to see deflections from the fibres. The spinner was turned off and propped up by some glass slides to give an appropriate clearance gap of approximately 2 mm above the electromagnet.

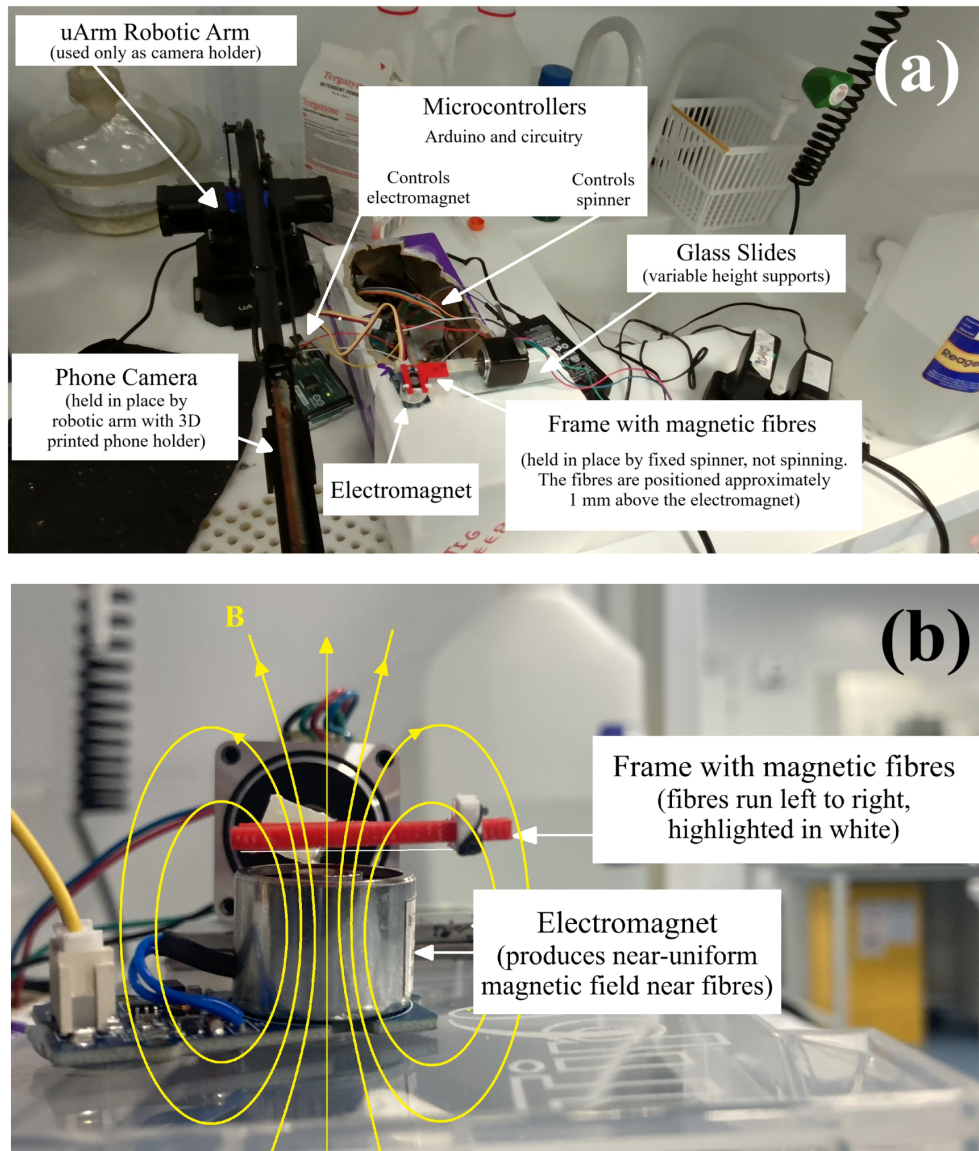


**Fig. 12. (a)** Overview of setup for testing deflection in a magnetic field. **(b)** Same setup, from the perspective of the phone camera, with the horizontally-oriented undeflected fibre made visible.

The frame (red in Figure 12(b)) was held horizontally at rest, with the slider (white in Figure 12(b)) at its ends, initially at full extension. A video was started and the electromagnet circuit was turned on, and five successive deflections (if visible) were observed on video before stopping. The video could then be analysed for the deflection and angle of deflection at the ends by screenshotting at key frames and reading from pixel measurements in the simple graphics editor software MS Paint. In theory, these calculations might be automated using computer vision (e.g. Python's `opencv` module) but this was deemed overcomplicated when the small number of images could more easily be processed manually.

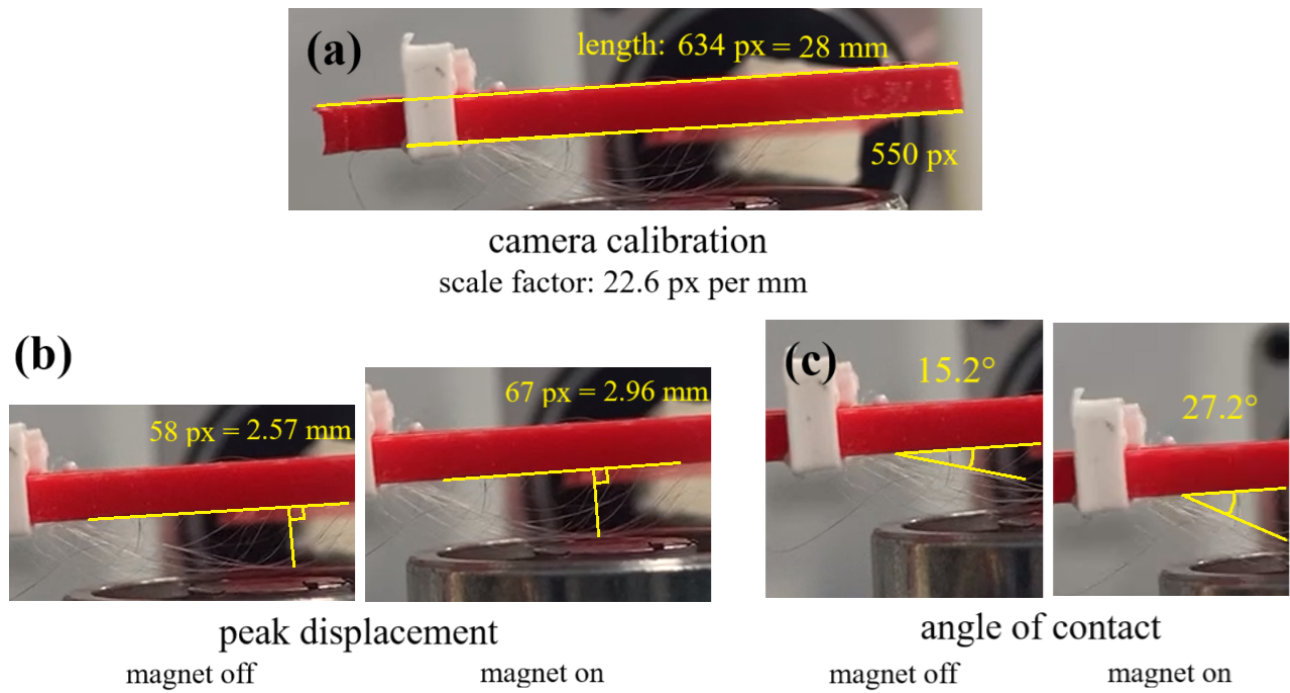


**Fig. 13. (a)** The scale factor for pixels to millimetres is determined by finding the distance along the full length of the frame in the image (frame is 28 mm long). The distance of the slider is also found and evaluated using this scale factor (e.g. 550 px = slider is at 24.3 mm). **(b)** Perpendicular lines to the frame are drawn to the point where the fibres converge in the image, at their peak displacement, and the length of this line segment is measured and converted to mm using the scale factor found above. **(c)** Tangent lines are drawn parallel to the fibres closest to the frame and the angle is computed using trigonometry from the pixel coordinates.

## Preparing Hydrogels

The following procedure was used to prepare each fibre solution:

1. To a clean measuring cylinder, pour out 50 ml of DI water; transfer to a small beaker.
2. Place a clean dry weighing boat on a balance; tare the balance.
3. Using a spatula, weigh out the appropriate masses of gelatin and sodium alginate powder into the weighing boat. Add the contents to the beaker of DI water.
4. Drop in a large magnetic stir bar and label the beaker.
5. Place the beaker on a hot plate at 80 °C and stir at moderate power for 1 hour.
6. Remove the stir bar and transfer the beaker to a refrigerator. Once cooled to room temperature, the hydrogel will crosslink itself and transition to the single solid phase.
7. When the hydrogel is ready for use, transfer the beaker containing the solid hydrogel to an oven at 80 °C for approximately 10 minutes to melt the hydrogel into the liquid state.
8. The liquid hydrogel formulation can now be added to e.g. the 3D bioprinter or an uncapped syringe for manual deposition onto the fibres. The hydrogel will naturally solidify again as it equilibrates to room temperature.

Table 4 shows the three hydrogel compositions trialled in this project. It was found that when hydrogel (A) was added to the frame, the whole frame became too rigid for the fibres to move: they were effectively frozen in place. More compliant hydrogels were necessary for observable actuation, and (B) was found as the minimal concentration such that the UCST (i.e. solidification temperature) of the gelatin-alginate hydrogel was just above room temperature, ensuring a mechanically flexible hydrogel. Composition (C) was too dilute to form a hydrogel, with its UCST close to the freezing point of water, remaining in its gel (two-phase liquid) state down to room temperature, and so could not be used with any fibres.

Identifier	Gelatin, wt%	Alginate, wt%	Solvent
(A)	6	1	DI water
(B)	2	0.333	DI water
(C)	0.25	0.083	DI water

**Table 4.** Compositions of three hydrogels tested, (A), (B) and (C).

## Preparing the Fibre-Hydrogel Composites

Once the desired fibres have been spun and the hydrogels prepared, combining them together is very straightforward, and can be done manually or using a 3D printer. In this project, to save time, the composites shown in images in this report were done by hand, but the in-house 3D bioprinter Printer.HM was also able to easily print the hydrogel, ideal if using a cell culture.

1. Draw up 0.65 ml of warm liquid phase hydrogel into a 18-gauge needle-capped syringe. This can be performed shortly after removing from the oven due to the rapid natural cooling to ambient temperature.
2. Inject the hydrogel carefully on top of the fibres, one drop at a time. The high surface tension of the hydrogel can be exploited by forming small beads on the surface and joining them together to fill out the whole area above the fibres. Ensure that a small region near the slider is left clear.
3. Wait for approximately 10 minutes for the hydrogel to solidify on the fibres. The hydrogel can be gently pressed with a non-stick surface to ensure good adherence.

## Testing the Fibre-Hydrogel Composites for Magnetic Responsiveness

Due to the damage induced by testing the flexibility of the pure fibres (shown in Figure 13(a)), a new set of fibres was spun from the same solutions when testing the fibres with the hydrogel. The solution (contained within a small vial) was reheated at 50 °C on a hot plate and the magnetic stirring was turned on. No stir bars were inside the vials, but the magnetic solutions were able to spin to some extent on their own. This was performed to solubilise any precipitated polymer ‘blobs’ which were observed to develop from dried-out solutions, although visibility was obscured by the opaque black iron oxide coating on the vial interior. To save time, these were spun by hand by manually extruding from a 25-gauge blunt-tipped syringe. Due to developing more practice throughout the course of the project, the hand-spinning technique had improved in quality significantly from that shown in Figure 11.

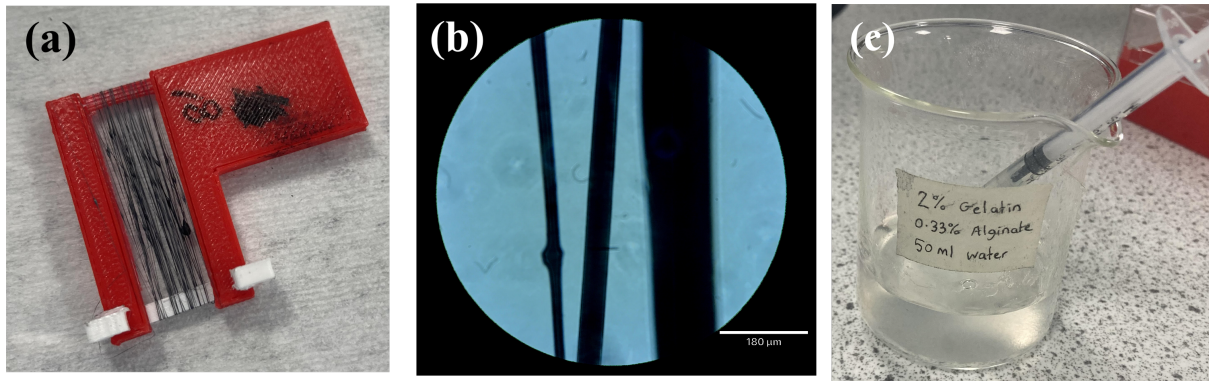


**Fig. 12.** (a) New fibres spun by hand (no spinner, no robot arm, no added hydrogel) using Composition (8), after reheating the solution at 50 °C for 10 minutes with gentle stirring. (b) Microscopy of hand-spun fibres from Composition 8, showing larger-than-normal variation in fibre thickness (scale bar: 180  $\mu\text{m}$ ) and a small blob on one of the fibres is visible. (c) Hydrogel (2) in its solid state, to be heated before deposition onto the fibres.

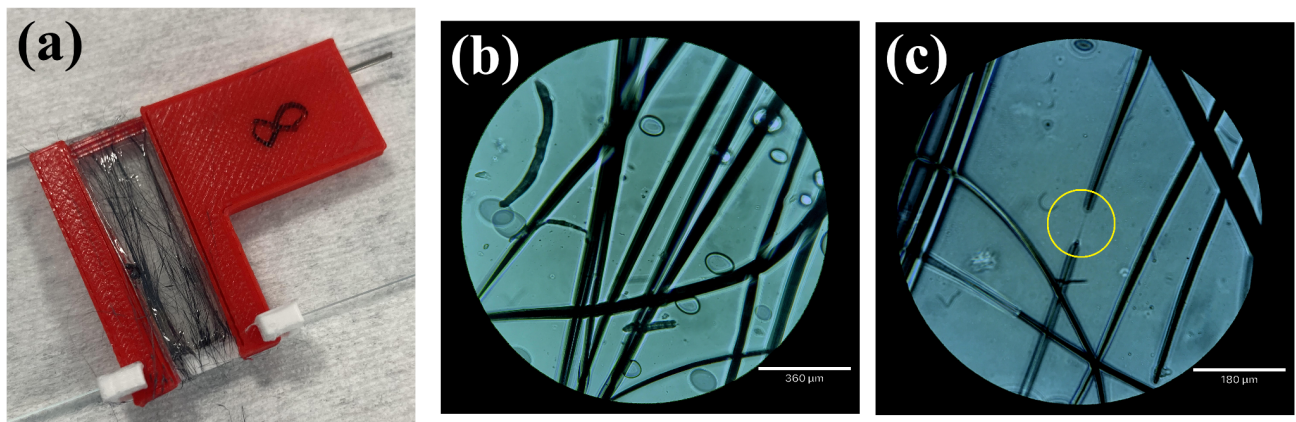


**Fig. 13.** (a) The old fibres from Composition (8) were severely frayed after repeatedly changing the length (by moving the white slider) and actuating with the magnet, then ‘freezing’ with hydrogel (1), giving a very rigid composite with no practical use. (b) Microscopy at 10 $\times$  resolution (scale bar: 360  $\mu\text{m}$ ) of these fibres, showing many defects and tangled fibres. (c) Another close-up at 20 $\times$  resolution (scale bar: 180  $\mu\text{m}$ ). In the yellow circled region, the fibre has become partially uncoated, losing a section of the iron oxide sheath and leaving a tiny barely-visible strand of polystyrene (diameter  $\sim 1 \mu\text{m}$ ).

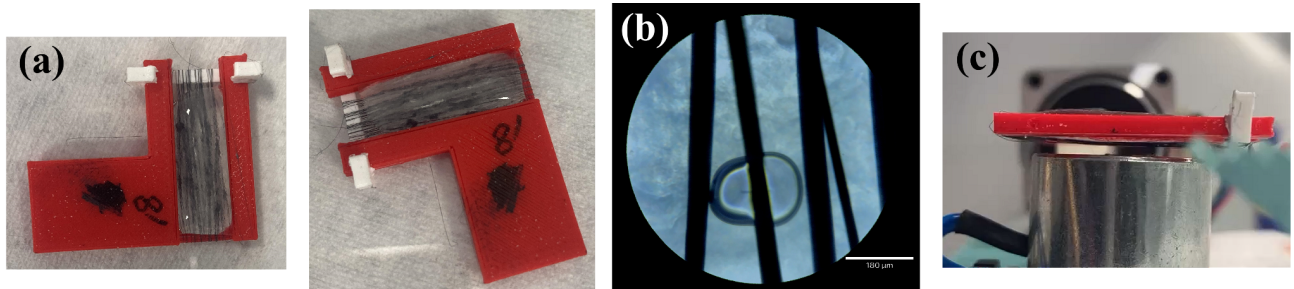


**Fig. 14.** (a) The hydrogel-fibre composite, using the new Composition (8) and hydrogel (2). The slider is in the fully extended position. (b) Microscopy of the fibre-hydrogel composite, observed from above. The scale bar reads  $180\text{ }\mu\text{m}$ . A tiny spherical air bubble in the hydrogel is visible. (c) The fibre-hydrogel composite on the frame ready for testing with the electromagnet. The fibres are along the bottom and the hydrogel extends up to the top.

---

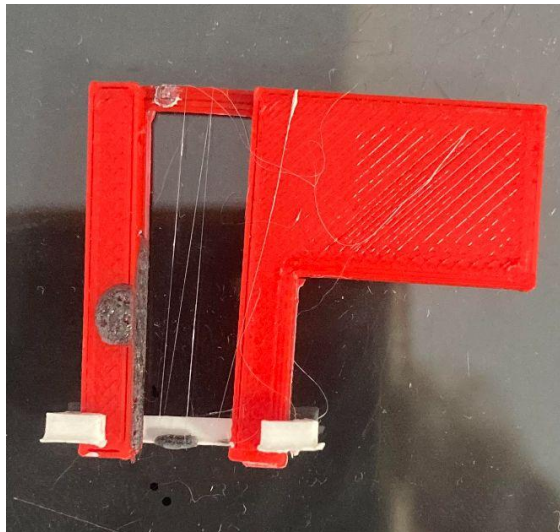
⑤      **Results and Discussion**

---

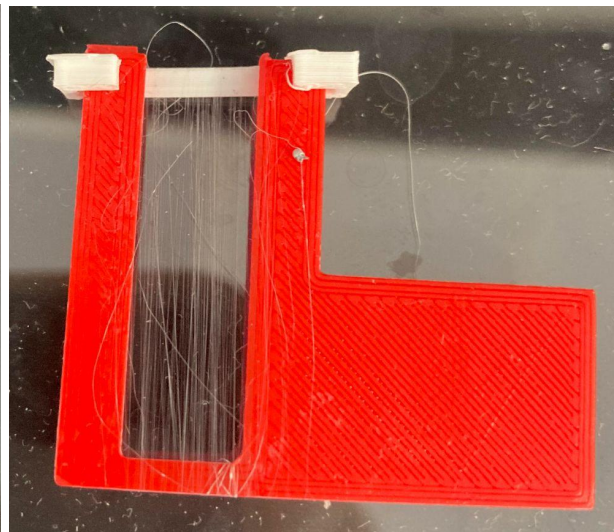
### 5.1. Analysis of Results

#### Spun Fibres

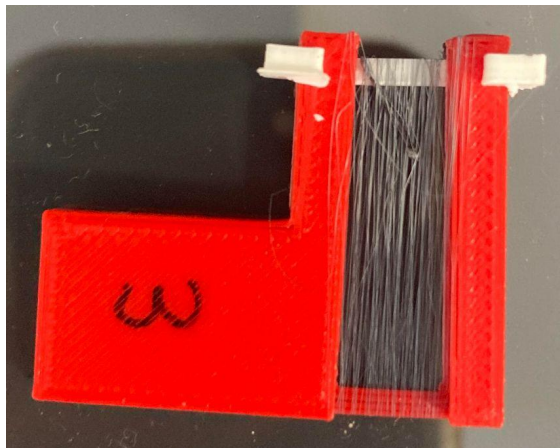
The fibres from each composition (1)-(9) (defined in Table 3) were spun at full length.



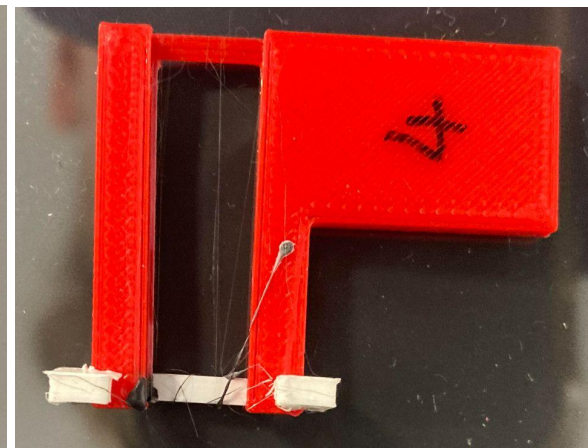
**Composition (1)**  
**10% Polystyrene, 10% Iron Oxide**



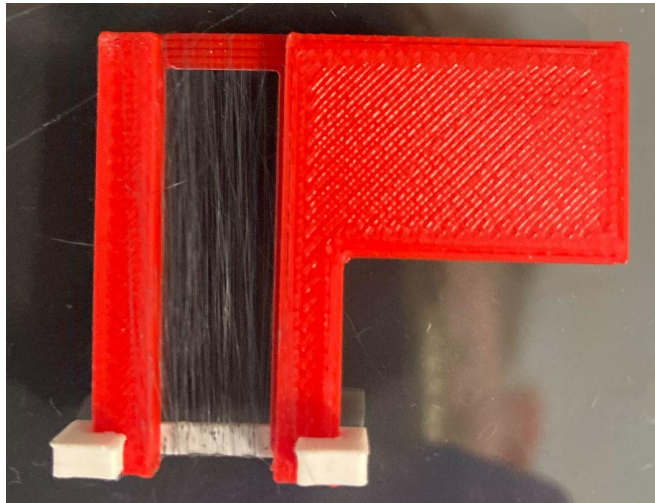
**Composition (2)**  
**20% Polystyrene, 10% Iron Oxide**



**Composition (3)**  
**30% Polystyrene, 10% Iron Oxide**



**Composition (4)**  
**10% Polystyrene, 20% Iron Oxide**



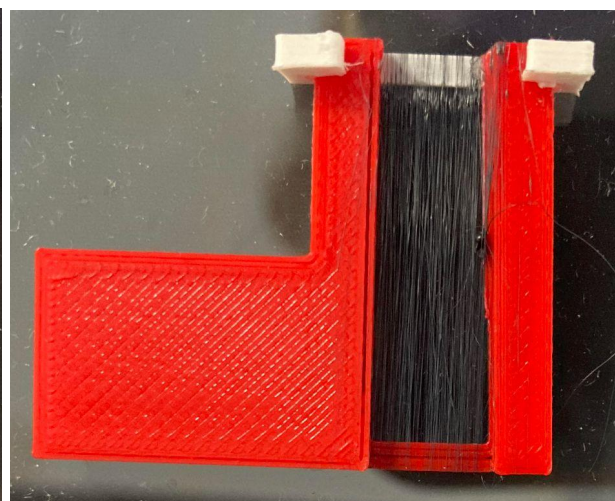
**Composition (5)**  
**20% Polystyrene, 20% Iron Oxide**



**Composition (6)**  
**30% Polystyrene, 20% Iron Oxide**



**Composition (7)**  
**10% Polystyrene, 30% Iron Oxide**

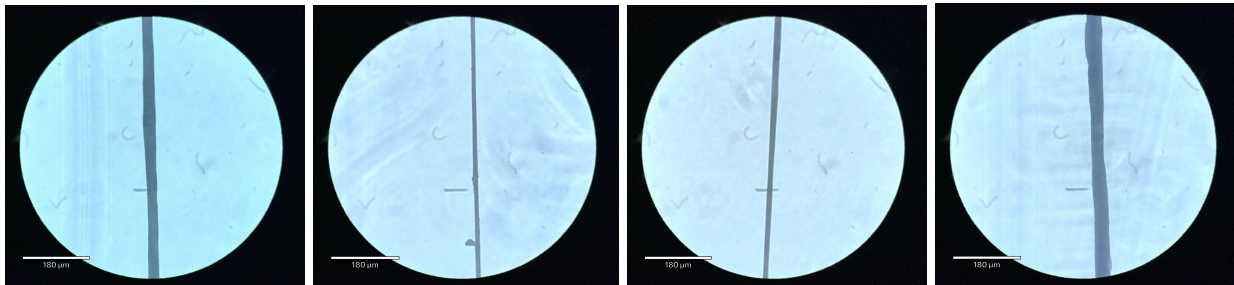


**Composition (8)**  
**20% Polystyrene, 30% Iron Oxide**

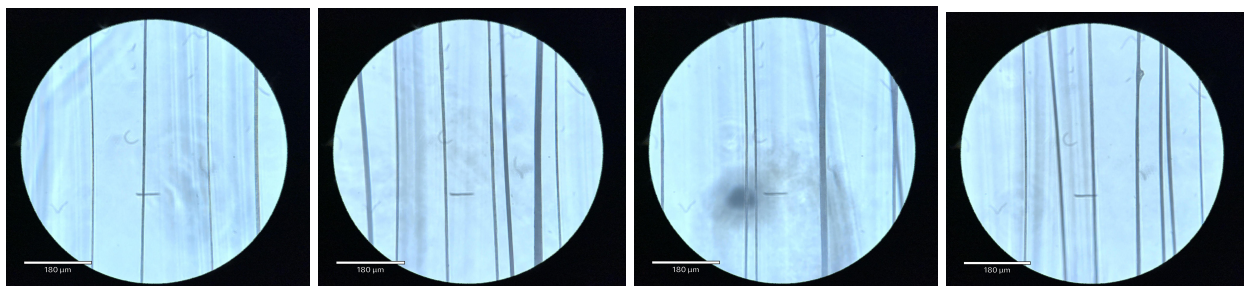
Visually, compositions (3), (5), (6), (7) and (8) produced good-quality fibres. (1) and (4) were extremely fragile and broke off rapidly during extrusion. (2) was also fragile but a little better. The solvent solution used to produce Composition (9) (30% Polystyrene, 30% Iron Oxide) was a practically-solid solution from which drawing up any remaining solvent into the syringe was infeasible, even when reheated to 80 °C. Therefore, no fibres could be spun from (9) and it was removed from the investigations.

## Microscopy and Characterisation

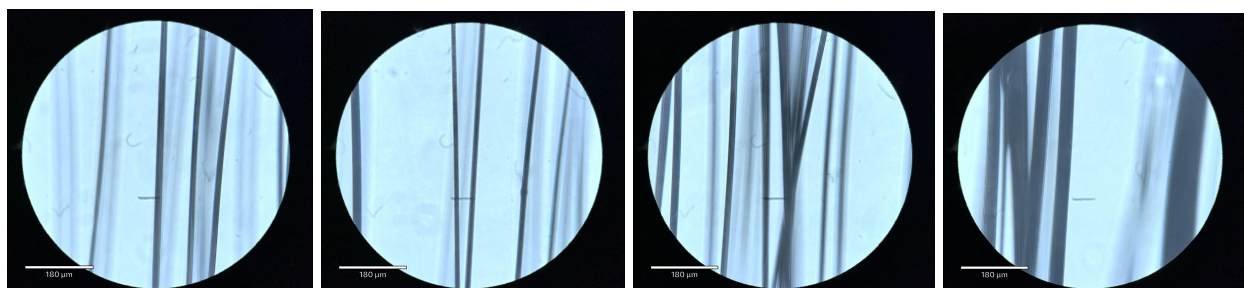
Light microscopy at 20 $\times$  magnification. The scale bar in all images reads '180  $\mu\text{m}$ '.



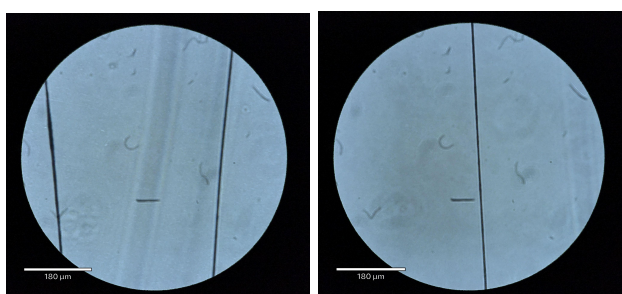
**Composition (1): 10% Polystyrene, 10% Iron Oxide**



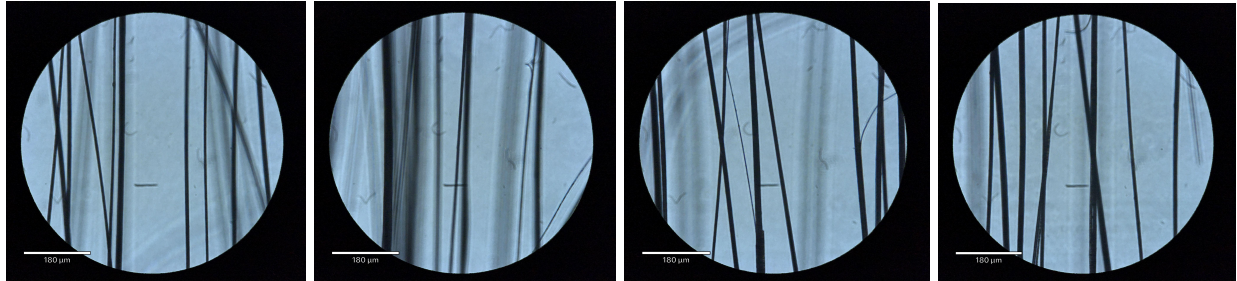
**Composition (2): 20% Polystyrene, 10% Iron Oxide**



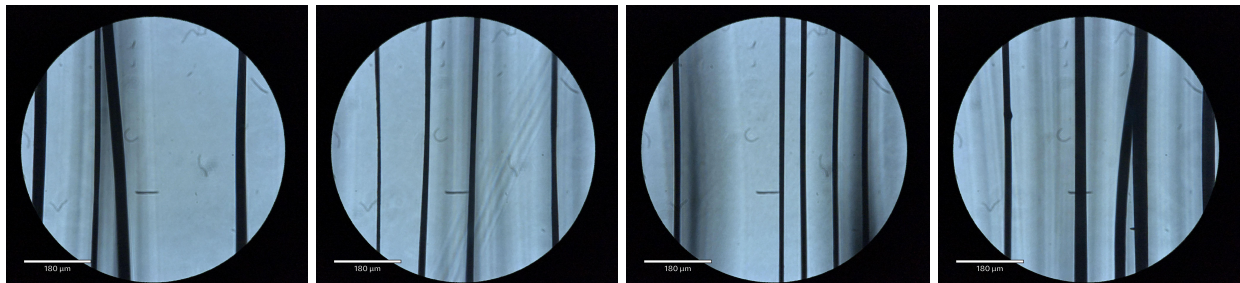
**Composition (3): 30% Polystyrene, 10% Iron Oxide**



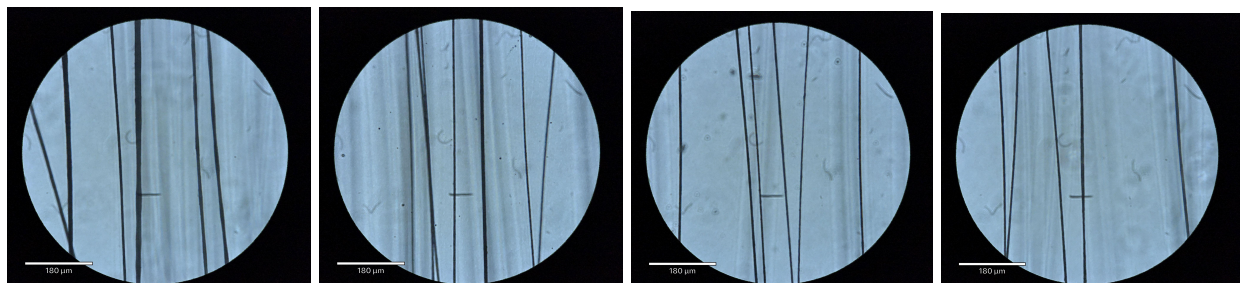
**Composition (4): 10% Polystyrene, 20% Iron Oxide**



**Composition (5): 20% Polystyrene, 20% Iron Oxide**



**Composition (6): 30% Polystyrene, 20% Iron Oxide**



**Composition (7): 10% Polystyrene, 30% Iron Oxide**



**Composition (8): 20% Polystyrene, 30% Iron Oxide**

As mentioned, Composition (9) yielded no fibres.

## Fibre Widths

Some additional microscopy photos other than those shown above were taken to gather more data, and each image was randomly sampled, forming a dataset of the widths of the fibres from each sample, collecting 10 data points for each composition.. The bar charts in Figure 14 show the mean and standard deviations (as error bars).

Number of samples	Mean	Standard deviation	Minimum	Maximum
80	14.8 $\mu\text{m}$	8.7 $\mu\text{m}$	4.1 $\mu\text{m}$	40.0 $\mu\text{m}$

**Table 5.** Summary statistics for the whole dataset of fibre diameters.

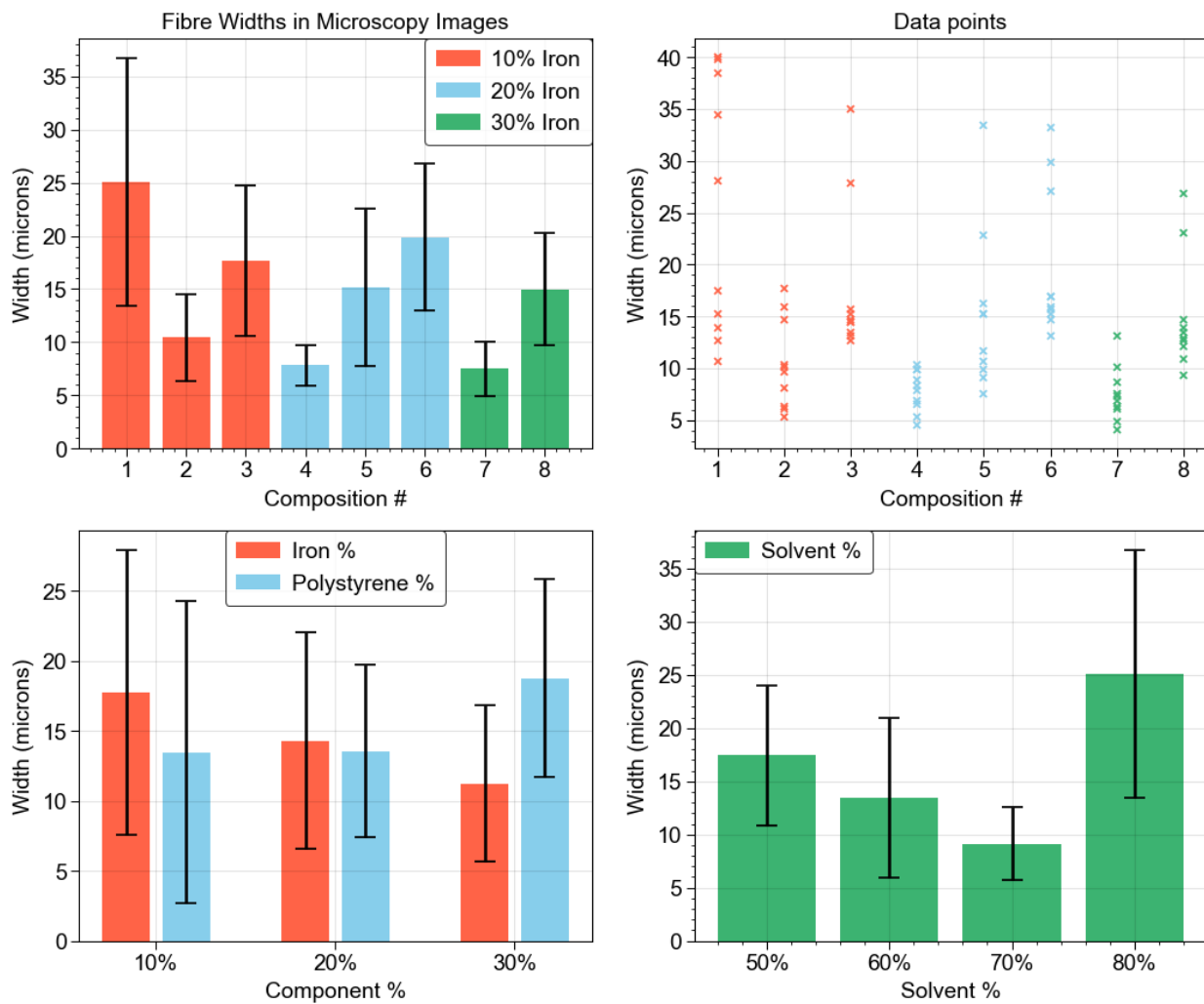
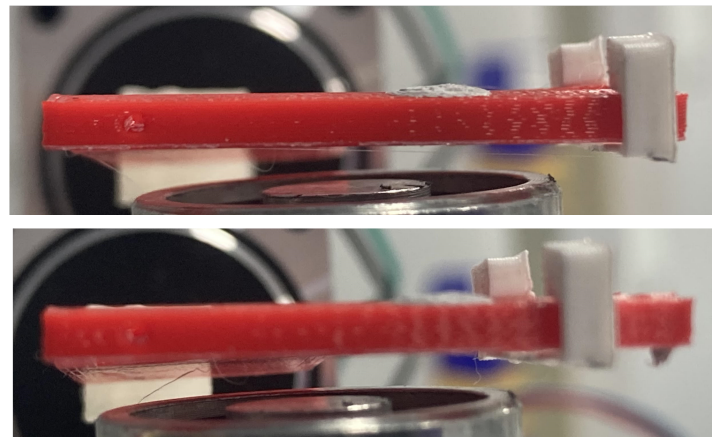


**Fig. 14.** Data showing the variation of fibre diameter for all compositions, before the addition of any hydrogel and before testing for magnetic response. The error bars show plus or minus one standard deviation for each group.

### Fibre Magnetic Actuation (No Hydrogel)

Each frame was held above the electromagnet. In the photo below of testing Composition (1), the **top** image shows the frame at fully extended length, at which deflection is minimal (invisible). The **bottom** image then shows the frame with the slider slightly contracted by approximately 1-3 mm, and the measurements are analysed.

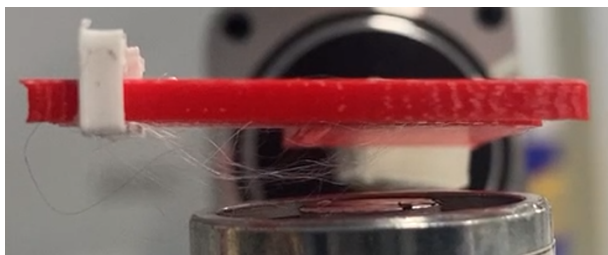


**Compositions (1) and (4)** (effectively the same response, too fragile to investigate)

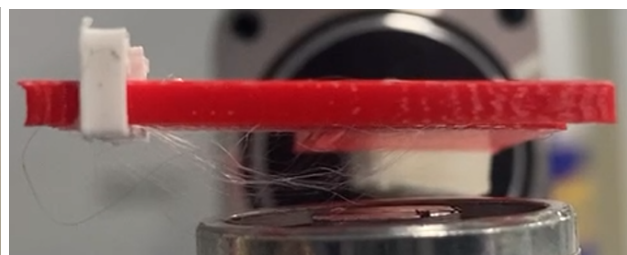
In each of the following, the slider was contracted a very small distance and photos were taken during the period when the electromagnet was on and off. The motion can be better observed on video, but analysis of the photos is also used to quantitatively determine deflections and angles.



Fully extended, electromagnet **on/off** (no visible deflection)

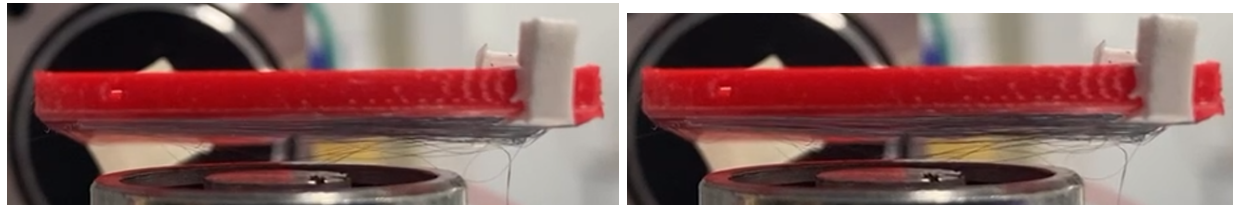
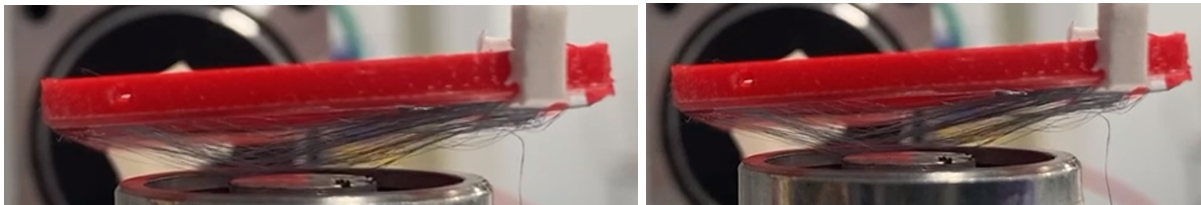
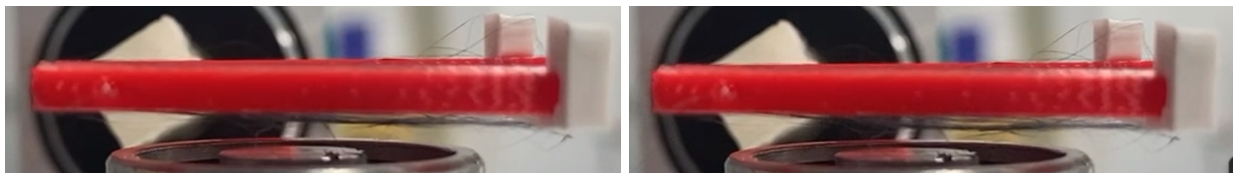
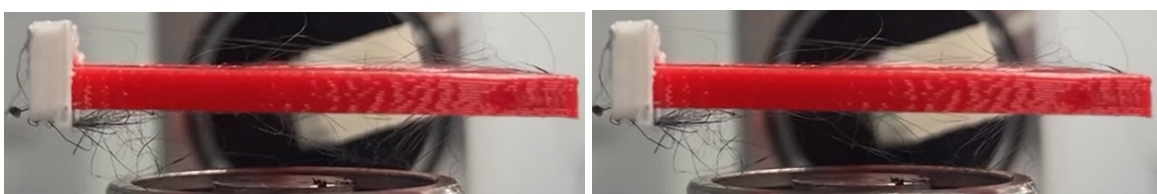
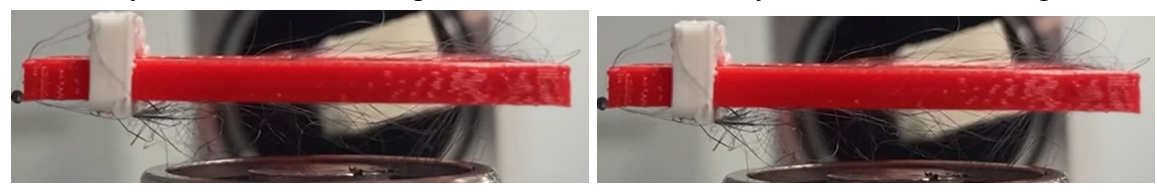


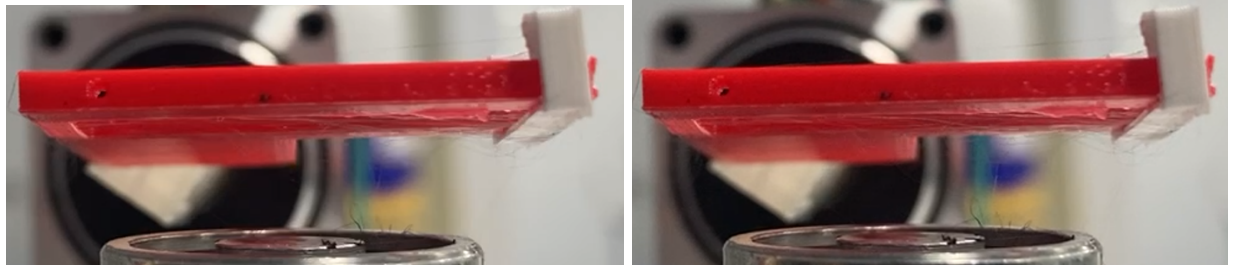
Contracted, electromagnet **off**



Contracted, electromagnet **on**

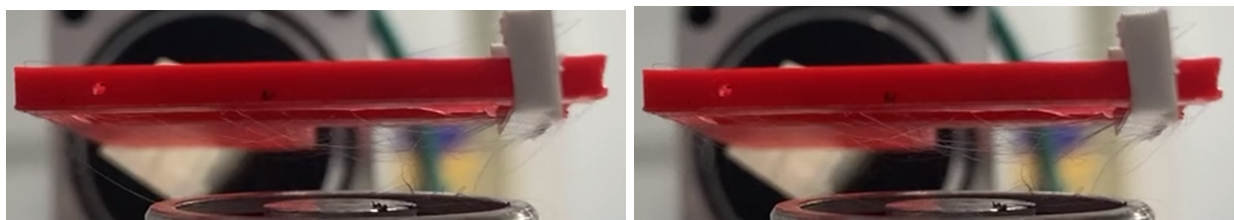
**Composition (2)** (also poor quality, but deflection is observed without breakage)

Fully extended, electromagnet **off**Fully extended, electromagnet **on**Contracted, electromagnet **off**Contracted, electromagnet **on****Composition (3)**Fully extended, electromagnet **off**Fully extended, electromagnet **on**Contracted, electromagnet **off**Contracted, electromagnet **on****Composition (5)**Fully extended, electromagnet **off**Fully extended, electromagnet **on**Contracted, electromagnet **off**Contracted, electromagnet **on****Composition (6)** (unfortunately fibres became damaged due to experimental error)



Fully extended, electromagnet off

Fully extended, electromagnet on



Contracted, electromagnet off

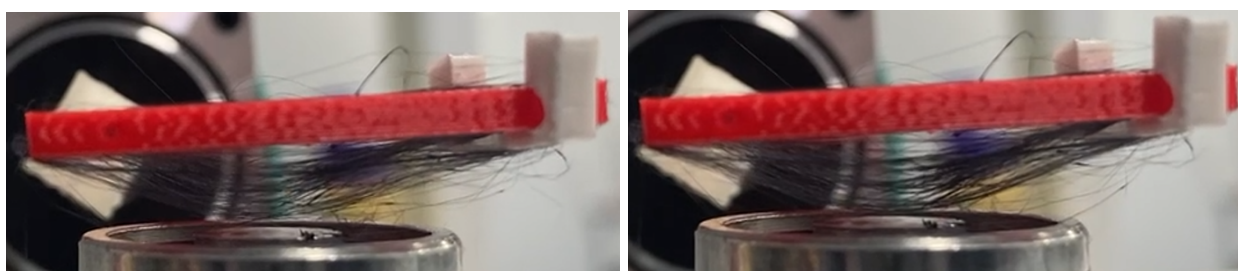
Contracted, electromagnet on

**Composition (7)** (thin fibres are hard to see, but actuation is clear on video)



Fully extended, electromagnet off

Fully extended, electromagnet on



Contracted, electromagnet off

Contracted, electromagnet on

**Composition (8)** (very clear actuation, best performing fibres)

### Maximum Displacements and Angles of Contact of Fibres (No Hydrogel)

Videos were captured of each set of fibres, switching the electromagnet on and off every second. The peak deflection of the fibres and the angle of contact with the supports of the frame were recorded by counting pixel distances on the images at each ‘on’ and ‘off’ interval, providing a data point for each variable per one second of video. Since sample (1) and (6) were destroyed by the magnet, it could not be recorded. (4) remained intact and could be measured albeit with only one single fibre and its angle could not be measured. The results are shown in Figure 15.

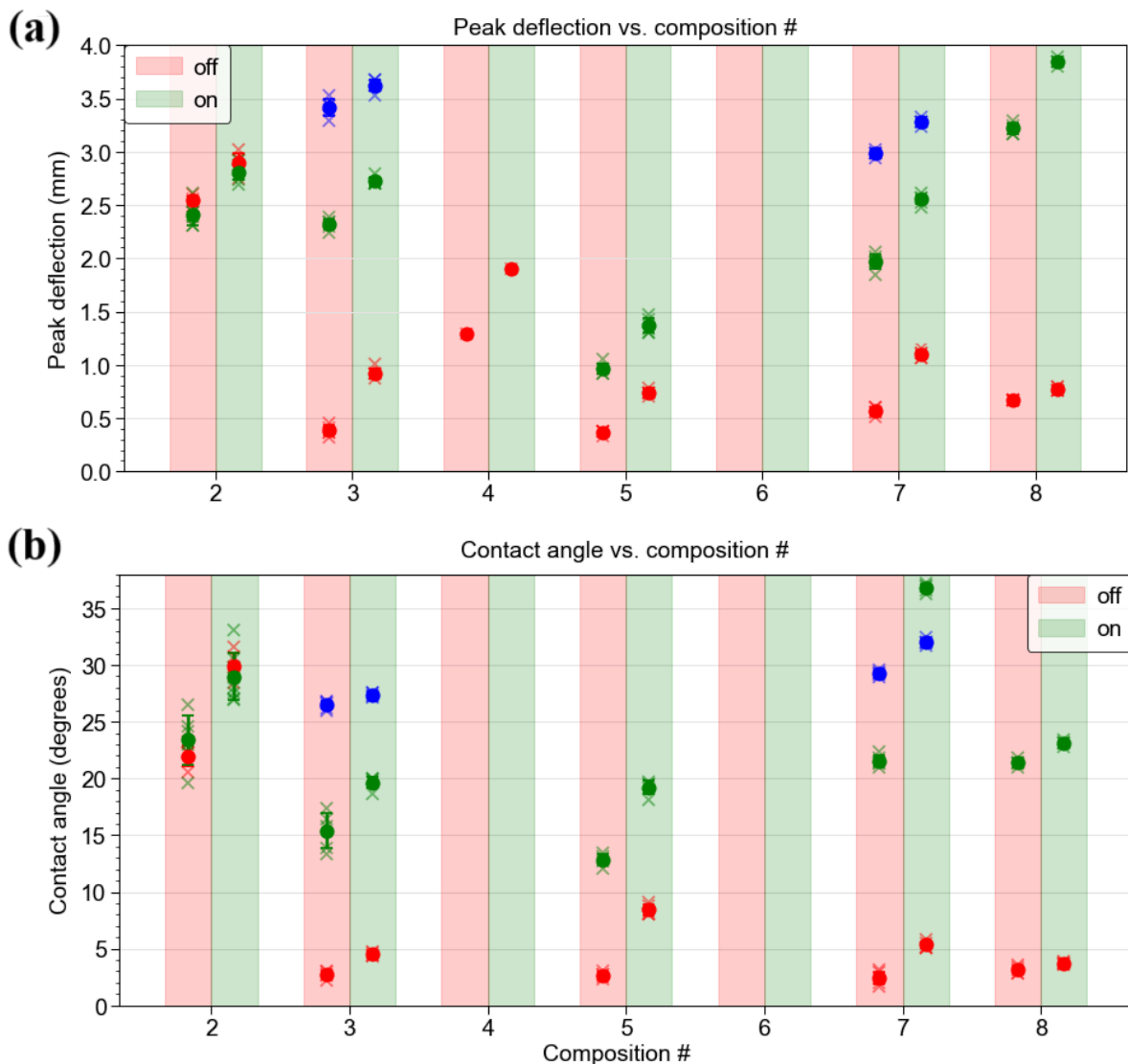


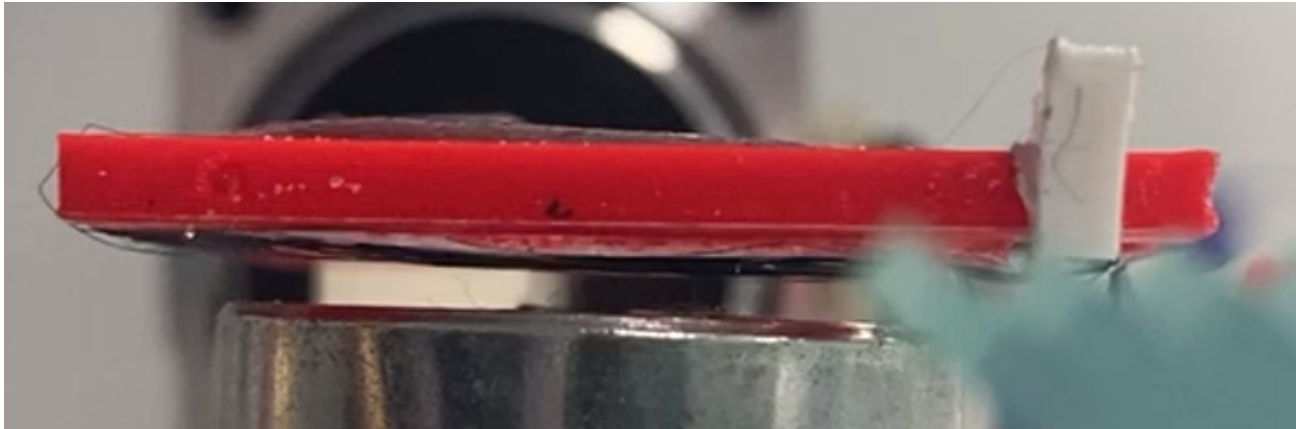
**Fig. 15. (a)** Peak deflections and **(b)** contact angle with supports of the fibres of each composition, with red and green columns for electromagnet ‘off’ and ‘on’ respectively, shown as  $N = 5$  data points ( $\times$ ) as well as mean ( $\bullet$ ) and standard deviation as error bars. The key to the marker colour (represents different slider distances) is given in Table 5.

Colour	Composition #						
	2	3	4	5	6	7	8
red	24.39	26.63	28.00	28.00		27.66	27.85
green	25.38	25.84		26.28		25.86	27.15
blue		23.44				25.94	

**Table 5.** Fibre horizontal length (distance to slider) in mm, corresponding to the datasets of each marker colour in Figure 15. For example, the red markers in Composition (2) were collected at a slider distance of 24.39 mm.

**Fibre Magnetic Actuation (With Hydrogel)**

The new fibres from Composition (8) with hydrogel (2) were actuated. As before, the photo format makes direct comparison visually difficult but the actuation is very clear on video.



Fully extended, electromagnet **off**



Slightly contracted, electromagnet **off**



Slightly contracted, electromagnet **on**

It is noted that the fibres are pulled down towards the electromagnet to a lesser extent than without the hydrogel, as predicted by the theoretical composite model discussed in Section 3.1. Additionally, it can be seen that, by observing the top section of the frame, the hydrogel is also pulled down by a similar distance as the fibres, indicating that the composite indeed moves as a collective unit, without delamination of the fibres from the hydrogel matrix. This also verifies the feasibility of actuating the hydrogel remotely since the fibres are not in physical contact with the electromagnet at any point during the motion.

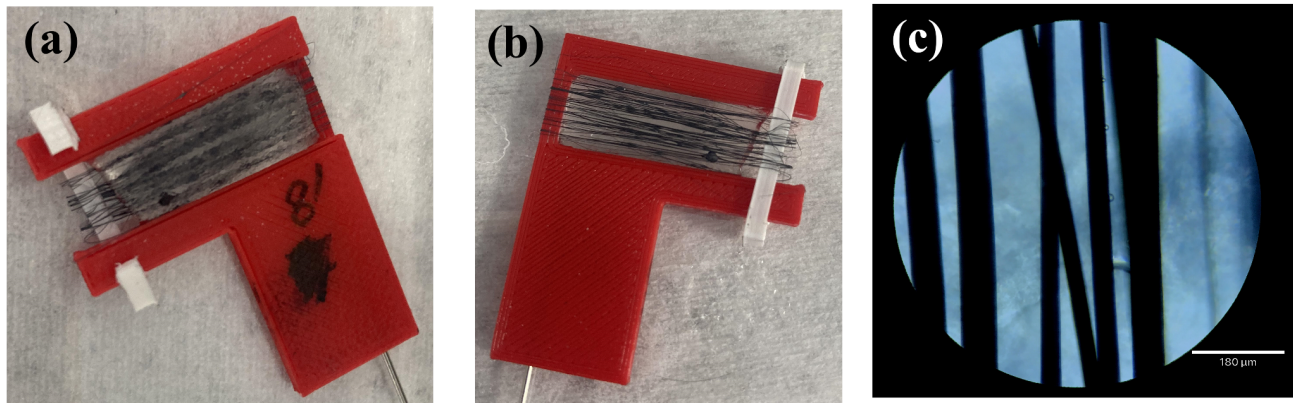


**Fig. 16.** (a) The frame containing the fibre-hydrogel composite after performing the actuation tests. The quality of the fibres is retained, unlike in the case without the hydrogel, where the testing step significantly degraded the fibres. The hydrogel has not shifted position and the slider is still in the slightly contracted position, so the fibres around the edge are a little loose, but are easily straightened up by pulling the slider back gently to the fully extended position. (b) The bottom side of the frame, showing that the fibres are still fully intact on both sides. (c) Microscopy confirms that the fibres are still of good quality, without breakage. Some tiny air bubbles in the hydrogel are still present, similar to before testing (as seen in Figure 14).

### Angles and Deflection and Maximum Displacements of Fibres (With Hydrogel)

A total of 40 seconds of video was captured of the fibres from Composition (8) with hydrogel (2), providing 20 measurements each where the electromagnet was ‘on’ and ‘off’ respectively, allowing for analysis of the change in peak displacement and change in contact angle with the supports for both the fibres (bottom of the frame) and the hydrogel (top of the frame). The results are shown in Figure 17. The fibres were spun at a length of 26.5 mm and the slider was contracted by 1.0 mm to a distance of 25.5 mm where all measurements below were taken.

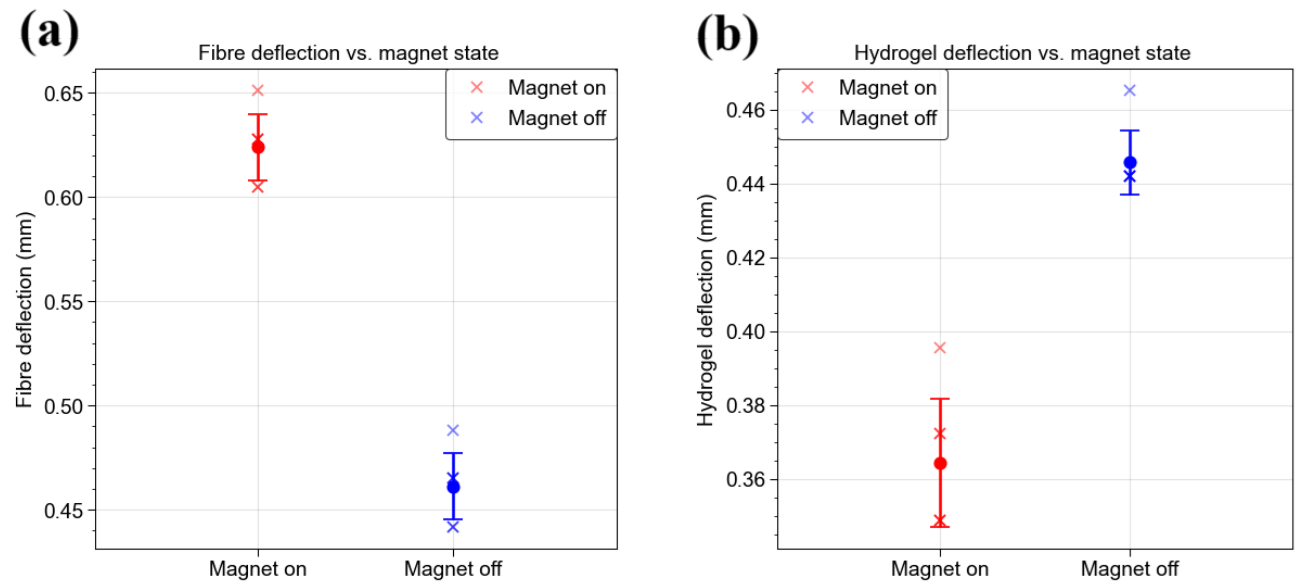


**Fig. 17. (a)** Peak deflection of the fibres observed at the bottom of the frame. **(b)** Peak deflection of the hydrogel observed at the top of the frame. In both,  $N = 6$  data points were collected for each case (magnet on and off).

The change in peak displacement caused by the magnet is shown in Table 6. It is observed that the mean displacement of the hydrogel is approximately half that of the fibres, suggesting that the hydrogel partially deforms as well as the fibres.

Fibres		Hydrogel	
Mean	Standard deviation	Mean	Standard deviation
0.163 mm	0.027 mm	0.081 mm	0.012 mm

**5.2. Discussion**

⑥ **Conclusions**

---

**6.1. Primary Findings**

**6.2. Future Work**

- 
- [1] Utech, S., & Boccaccini, A. R. (2015). A review of hydrogel-based composites for biomedical applications: enhancement of hydrogel properties by addition of rigid inorganic fillers. *Journal of Materials Science*, 51(1), 271–310. <https://doi.org/10.1007/s10853-015-9382-5>
- [2] Liu, J., Garcia, J., Leahy, L. M., Song, R., Mullarkey, D., Fei, B., Dervan, A., Shvets, I. V., Stamenov, P., Wang, W., O'Brien, F. J., Coleman, J. N., & Nicolosi, V. (2023). 3D printing of multifunctional conductive polymer composite hydrogels. *Advanced Functional Materials*, 33(37). <https://doi.org/10.1002/adfm.202214196>
- [3] Brunsen, A., Utech, S., Maskos, M., Knoll, W., & Jonas, U. (2012). Magnetic composite thin films of  $\text{Fe}_x\text{O}_y$  nanoparticles and photocrosslinked Dextran Hydrogels. *Journal of Magnetism and Magnetic Materials*, 324(8), 1488–1497. <https://doi.org/10.1016/j.jmmm.2011.11.039>
- [4] Salahuddin, B., Aziz, S., Gao, S., Hossain, Md. S., Billah, M., Zhu, Z., & Amiralian, N. (2022). Magnetic hydrogel composite for wastewater treatment. *Polymers*, 14(23), 5074. <https://doi.org/10.3390/polym14235074>
- [5] Tang, S., Yan, Y., Lu, X., Wang, P., Xu, X., Hu, K., Yan, S., Guo, Z., Han, X., Zhang, F., & Gu, N. (2024). Nanocomposite magnetic hydrogel with dual anisotropic properties induces osteogenesis through the NOTCH-dependent pathways. *NPG Asia Materials*, 16(1). <https://doi.org/10.1038/s41427-024-00535-x>
- [6] Yang, L., Nandakumar, D. K., Miao, L., Suresh, L., Zhang, D., Xiong, T., Vaghasiya, J. V., Kwon, K. C., & Ching Tan, S. (2020). Energy harvesting from atmospheric humidity by a hydrogel-integrated ferroelectric-semiconductor system. *Joule*, 4(1), 176–188. <https://doi.org/10.1016/j.joule.2019.10.008>
- [7] Wang, Y., Zhang, W., Shan, Y., Yu, X., & Chen, K. (2023). Preparation of polyacrylamide/calcium alginate@ $\text{Ti}_3\text{C}_2\text{T}_x$  composite hydrogels with high adhesive performance for flexible supercapacitor electrolytes. *Colloids and Surfaces A: Physicochemical and Engineering Aspects*, 666, 131312. <https://doi.org/10.1016/j.colsurfa.2023.131312>
- [8] Thoniyot, P., Tan, M. J., Karim, A. A., Young, D. J., & Loh, X. J. (2015). Nanoparticle–Hydrogel Composites: Concept, design, and applications of these promising, Multi-Functional Materials. *Advanced Science*, 2(1–2). <https://doi.org/10.1002/advs.201400010>

- [9] Simińska-Stanny, J., Nizioł, M., Szymczyk-Ziółkowska, P., Brożyna, M., Junka, A., Shavandi, A., & Podstawczyk, D. (2022). 4D printing of patterned multimaterial magnetic hydrogel actuators. *Additive Manufacturing*, 49, 102506. <https://doi.org/10.1016/j.addma.2021.102506>
- [10] Kokol, V., Pottathara, Y. B., Mihelčič, M., & Perše, L. S. (2021). Rheological properties of gelatine hydrogels affected by flow- and horizontally-induced cooling rates during 3D cryo-printing. *Colloids and Surfaces A: Physicochemical and Engineering Aspects*, 616, 126356. <https://doi.org/10.1016/j.colsurfa.2021.126356>
- [11] Imura, Y., Hogan, R. M. C., & Jaffe, M. (2014). Dry spinning of synthetic polymer fibers. Advances in Filament Yarn Spinning of Textiles and Polymers, 187–202. <https://doi.org/10.1533/9780857099174.2.187>
- [12] Turek, K., & Opila, J. (1990). Magnetic fibers. *Journal of Magnetism and Magnetic Materials*, 83(1–3), 279–280. [https://doi.org/10.1016/0304-8853\(90\)90515-r](https://doi.org/10.1016/0304-8853(90)90515-r)
- [13] Banerjee, H., Leber, A., Laperrousaz, S., La Polla, R., Dong, C., Mansour, S., Wan, X., & Sorin, F. (2023). Soft multimaterial magnetic fibers and textiles. *Advanced Materials*, 35(33). <https://doi.org/10.1002/adma.202212202>
- [14] Wu, S., Hu, W., Ze, Q., Sitti, M., & Zhao, R. (2020). Multifunctional Magnetic Soft Composites: A Review. *Multifunctional Materials*, 3(4), 042003. <https://doi.org/10.1088/2399-7532/abcb0c>
- [15] Derby, N., & Olbert, S. (2010). Cylindrical magnets and ideal solenoids. *American Journal of Physics*, 78(3), 229–235. <https://doi.org/10.1119/1.3256157>
- [16] Maldonado-Camargo, L., Unni, M., & Rinaldi, C. (2017). Magnetic characterization of iron oxide nanoparticles for biomedical applications. *Methods in Molecular Biology*, 47–71. [https://doi.org/10.1007/978-1-4939-6840-4\\_4](https://doi.org/10.1007/978-1-4939-6840-4_4)
- [17] Dillard, D. A., Mukherjee, B., Karnal, P., Batra, R. C., & Frechette, J. (2018). A review of Winkler's foundation and its profound influence on adhesion and soft matter applications. *Soft Matter*, 14(19), 3669–3683. <https://doi.org/10.1039/c7sm02062g>
- [18] Kurowiak, J., Kaczmarek-Pawelska, A., Mackiewicz, A., Baldy-Chudzik, K., Mazurek-Popczyk, J., Zaręba, Ł., Klekiel, T., & Będziński, R. (2022). Changes in the mechanical properties of alginate-gelatin hydrogels with the addition of *Pygeum africanum* with potential application in urology. *International Journal of Molecular Sciences*, 23(18), 10324. <https://doi.org/10.3390/ijms231810324>

- [19] Liu, G., & Zhao, X. (2005). Electromechanochemical Behavior of Gelatin Hydrogel Under Electric Field. *Journal of Macromolecular Science, Part A*, 42, 51 - 59.  
<https://doi.org/10.1081/MA-200040958>.
- [20] Khosravi Maleki, F., KM Nasution, M., Gok, M. S., & Arab Maleki, V. (2022). An experimental investigation on mechanical properties of  $\text{Fe}_2\text{O}_3$  microparticles reinforced polypropylene. *Journal of Materials Research and Technology*, 16, 229–237.  
<https://doi.org/10.1016/j.jmrt.2021.11.104>

- [14] Lei, I. M., Sheng, Y., Lei, C. L., Leow, C., & Huang, Y. Y. (2022). A hackable, multi-functional, and modular extrusion 3D printer for soft materials. *Scientific Reports*, 12(1). <https://doi.org/10.1038/s41598-022-16008-6>
- [15] Du, Z., Ai, J., Zhang, X., Ma, Z., Wu, Z., Chen, D., Tao, G., & Su, B. (2020). Stretchable electromagnetic fibers for self-powered mechanical sensing. *Applied Materials Today*, 20, 100623. <https://doi.org/10.1016/j.apmt.2020.100623>
- [16] Grothe, T., Brikmann, J., & Ehrmann, A. (2016). PEO as spinnable polymer and spinning-agent for non-spinnable materials. In *Aachen-Dresden-Denkendorf International Textile Conference 2016*.

---

(8)      **Appendix**


---

### 8.1. Appendix I: Symbols

#### Notation (A $\alpha$ - $\Omega\omega$ , A $a$ -Z $z$ )

$\sigma_y$	yield stress
$E$	Young's modulus
$l$	fibre end-to-end length
$w$	transverse loading force per unit length

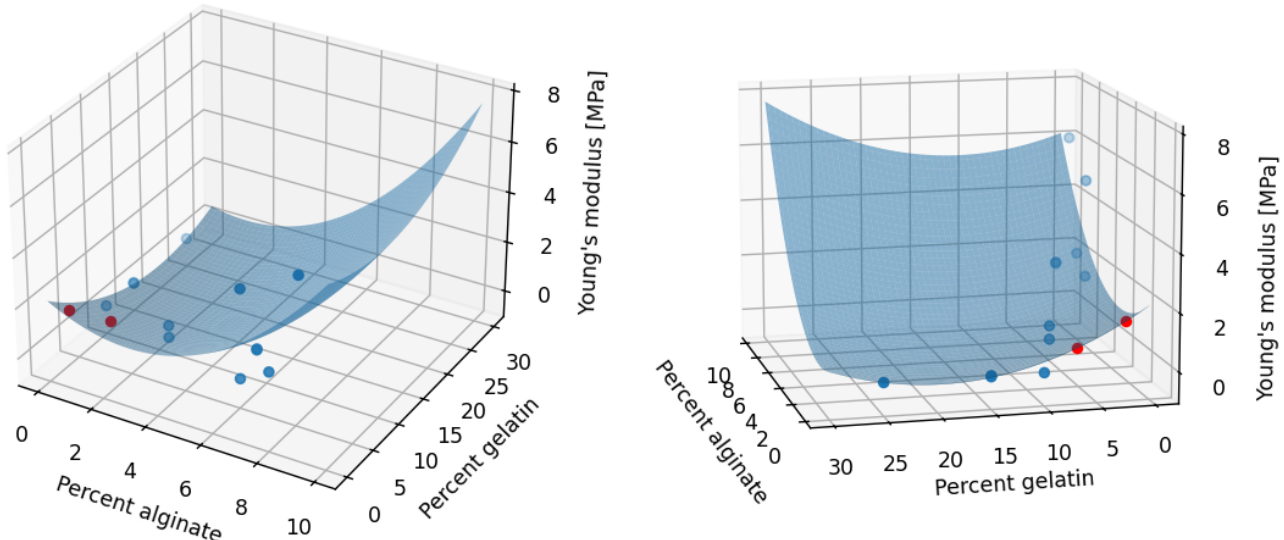
#### Abbreviations (A-Z)

3D	three dimensional
CAD	computer-aided design
CUED	Cambridge University Engineering Department
DI	deionised (water)
DMF	<i>N,N</i> -dimethylformamide
ECM	extracellular matrix
HEPA	high-efficiency particulate absorbing (filter)
LCST	lower critical solution temperature
MBSC	microbiological safety cabinet
PBS	phosphate-buffered saline
PEGDA	polyethylene glycol diacrylate
PEO	polyethylene oxide
PS	polystyrene
PU	polyurethane
SPION	superparamagnetic iron oxide nanoparticles
UCST	upper critical solution temperature
UDL	uniformly distributed load

## 8.2. Appendix II: Graphical and Tabular Data

### II.1. Predicted Young's Moduli of Gelatin-Alginate Hydrogels

Data was extracted from Table 1 in [18], excluding the last '30%, 65%' and 'human urethra' rows due to being an outlier and irrelevant respectively. Using Python's Scikit-learn library, a 2nd order (quadratic) linear regression was performed without regularisation on the full dataset to produce the model represented by the curved surface below. The model attained a root mean squared error of 0.98 MPa. The two data points marked in red are for (6% gelatin, 1% alginate) and (2% gelatin, 0.333% alginate), evaluated as 0.57 MPa and 1.55 MPa respectively, for two specific compositions tested in this project.



### 8.3. Appendix III: Code

The following Python (ver. 3.11) program was used to control the uArm robot arm while spinning the fibres onto the frame.

```

import os
import sys
import time
import threading

# import the uArm robot arm library
sys.path.append(os.path.join(os.path.dirname(__file__), "../.."))
from uarm.wrapper import SwiftAPI # robot arm library

# editable parameters
DEFAULT_POSITION = [250, 0, 115]
MOTION_RANGE = 8 # width of frame in mm to spin the fibres over
PRINTING_SPEED = 30 # rate of movement of robot arm from side to side
PRINTING_AXIS = 'y' # direction of movement
PRINT_TIME = 99999 # endless movement

# connect to the robot
swift = SwiftAPI(filters={"hwid": "USB VID:PID=2341:0042"})
swift.waiting_ready(timeout=3)
device_info = swift.get_device_info()
print(device_info)
firmware_version = device_info["firmware_version"]
if firmware_version and not firmware_version.startswith(("0.", "1.", "2.", "3.")):
    swift.set_speed_factor(0.0005)
swift.set_mode(0)

# move to default position
print('Moving to default position.')
swift.set_position(*DEFAULT_POSITION, speed=1000, wait=True)

# allow manual setting of the z-axis position (height above reference point in mm)
print('Minimum allowed z = -25 mm. Maximum allowed z = 160 mm.')
while True:
    pos = swift.get_position(wait=True, timeout=None, callback=None)
    print(f'Current (x, y, z) position (mm): {pos}.')
    entry = input("Adjust Z-axis position by how much (mm)? Press enter to continue. ")
    if entry == '':
        break
    else:
        try:
            new_z = pos[2] + float(entry)
            swift.set_position(pos[0], pos[1], new_z, speed=1000, wait=True)
        except (ValueError, TypeError):
            print("Invalid entry. Please enter a number to change the z-coordinate by in mm.")
            continue

# confirm ready to start print
pos = swift.get_position(wait=True, timeout=None, callback=None)
entry = input(f'Current z-axis position: {pos[2]}. Ready to start fibre printing, press "y" to')

```

```

go or anything else to exit. ')
if entry.lower() != 'y':
    print("Ending program.")
    exit(code=0)

def move_robot():
    i = 0
    t_start = time.time()
    while time.time() - t_start < PRINT_TIME:
        print(f'Starting pass {i+1}.')
        # move to other side
        if PRINTING_AXIS == 'x':
            swift.set_position(pos[0] - MOTION_RANGE, pos[1], pos[2], speed=PRINTING_SPEED,
wait=True)
        elif PRINTING_AXIS == 'y':
            swift.set_position(pos[0], pos[1] - MOTION_RANGE, pos[2], speed=PRINTING_SPEED,
wait=True)
        # move back
        swift.set_position(pos[0], pos[1], pos[2], speed=PRINTING_SPEED, wait=True)
        i += 1

robot_thread = threading.Thread(target=move_robot, daemon=True)
robot_thread.start()
robot_thread.join(timeout=PRINT_TIME)
print(f'Fibre printing complete after {PRINT_TIME} seconds. Moving to default position.')
swift.set_position(*DEFAULT_POSITION, speed=1000, wait=True)

```